

# From Microscopic Damage to Macroscopic Games: A Dimensionality Reduction of Stem Cell Homeostasis

Jiguang Yu<sup>1,2†</sup>, Louis Shuo Wang<sup>3\*†</sup>, Shihan Ban<sup>4†</sup>

<sup>1</sup>College of Engineering, Boston University, Boston, 02215, MA, USA.

<sup>2</sup>GSS Fellow of Institute for Global Sustainability, Boston University,  
Boston, 02215, MA, USA.

<sup>3</sup>Department of Mathematics, Northeastern University, Boston, 02115,  
MA, USA.

<sup>4</sup>Committee on Computational and Applied Mathematics, University of  
Chicago, Chicago, 60637, IL, USA.

\*Corresponding author(s). E-mail(s): [wang.s41@northeastern.edu](mailto:wang.s41@northeastern.edu);

Contributing authors: [jyu678@bu.edu](mailto:jyu678@bu.edu); [banshihan@uchicago.edu](mailto:banshihan@uchicago.edu);

†These authors contributed equally to this work as co-first authors.

## Abstract

Tissues must maintain macroscopic homeostasis despite the continuous microscopic accumulation of cellular damage. Theoretical models of this process often suffer from a disconnect between microscopic biophysics and macroscopic phenomenological games. Here, we bridge this gap by deriving an exact dimensionality reduction of a physiologically structured partial differential equation (PDE) into a low-dimensional dynamical system. Under the condition of uniform mortality, we mathematically demonstrate that tissue homeostasis operates as an induced Nash equilibrium, where the per-capita net growth rates of stem and differentiated phenotypes perfectly equalize. This reduction yields closed-form algebraic rules, the Ratio and Equalization Laws, that map continuous microscopic state dynamics to measurable macroscopic observables. To demonstrate the biological utility of this framework, we present a concrete, falsifiable case study of the murine intestinal crypt. By modeling crypt regeneration following irradiation-induced stem cell depletion, our framework successfully recovers the experimentally observed reliance on progenitor dedifferentiation. Furthermore, the model generates explicit, testable predictions, enabling the in vivo estimation of hard-to-measure lineage plasticity rates directly from aggregate static

cell counts. This work provides a rigorous, predictive mathematical foundation for understanding how fast-renewing tissues filter microscopic noise to sustain macroscopic regenerative capacity.

**Keywords:** Dimensionality reduction; Partial Differential Equations; Evolutionary game theory; Stem cell homeostasis; tissue homeostasis; stem cell plasticity.

## Author summary

How do our bodies maintain healthy organs when individual cells are constantly accumulating damage and dying? To survive, tissues rely on stem cells to replace lost tissue, and sometimes even allow mature cells to revert back into stem cells to help with emergency repairs. However, understanding exactly how tissues coordinate this complex balancing act has been historically difficult. Mathematical models usually focus either on the microscopic physical wear-and-tear of single cells or on the macroscopic "game" played by the whole cell population, but rarely both.

In this study, we bridge that gap. We developed a mathematical method that directly translates the complex physical rules of cell damage into a much simpler game-theory framework. We discovered that a healthy, stable tissue acts like a perfectly balanced game—a "Nash equilibrium"—where neither stem cells nor mature cells hold a competitive growth advantage over the other. By applying our theory to the rapid regeneration of the mouse intestine, we demonstrate that our equations can accurately predict how tissues heal after severe injury. Ultimately, our work provides biologists with a practical new tool: the ability to calculate hidden, complex tissue healing rates using only simple snapshot measurements of cell populations.

## 1 Introduction

Multicellular tissues face a fundamental conflict: they must preserve macroscopic stability (homeostasis) while individual cells continually accumulate molecular damage and drift toward disorder (Xavier Da Silveira Dos Santos and Liberali 2019; Guillot and Lecuit 2013). In rapidly renewing systems like the intestinal epithelium and hematopoietic system, stem and progenitor cells are continuously exposed to endogenous and environmental stressors (Chiacchiera 2019; Beumer and Clevers 2016). Over time, repeated challenges produce a broad cell-to-cell distribution of defects—ranging from DNA lesions to metabolic decline—that acts as a dynamic 'hidden coordinate' of damage. As this coordinate evolves, it reshapes intracellular signaling, biases fate choices, and undermines long-term tissue maintenance (Jones and Passegue 2023; McNeely et al. 2020; Chatterjee and Thakur 2021; Mi et al. 2022; Liu et al. 2022; Oh et al. 2014). More generally, reciprocal feedback in multiscale biological systems can generate not only homeostatic regulation but also explicit transitions to spatial niche formation and patterned heterogeneity in spatially extended settings (Yu et al. 2026a).

To cope with this heterogeneity, organisms exploit local regulatory feedback and cellular plasticity (Lou et al. 2019; Biteau et al. 2011; Bates et al. 2023). Differentiated

cells can revert to a proliferative stage through dedifferentiation to replace lost tissue (Jopling et al. 2011; Blanpain and Fuchs 2014). For example, following the ablation of native stem cells in the intestine or airway, committed progenitors can actively regain stem-like properties to repair the epithelium (Murata et al. 2020; Tata et al. 2013; Tetteh et al. 2016). Yet, this plasticity is a double-edged sword: while supporting repair, its misregulation can promote dysplasia or malignant transformation (Van Der Heijden and Vermeulen 2019; Beumer and Clevers 2016; Chiacchiera 2019), functioning effectively as a high-stakes strategy in the tissue’s struggle for survival (Bensellam et al. 2018; Nordmann et al. 2017).

## 1.1 The challenge of scale separation: Physics vs. Games

Understanding how tissues coordinate this plasticity requires bridging two theoretical scales. At the microscopic scale, physiologically structured partial differential equations (PDEs) capture continuous damage accumulation and division events (Magal and Ruan 2018; Perthame 2007; Cui et al. 2024; Zhang and Liu 2019). However, structured PDEs are mechanistic but hard to interpret; their infinite-dimensional nature obscures simple, testable laws for the whole tissue.

At the macroscopic level, evolutionary game theory elegantly models ecological mechanisms of tissue coordination (Zhu et al. 2016; Huang et al. 2015; Argasinski and Broom 2018; Helbing 1996). Yet, a critical gap remains: game-theoretic “payoff functions” are typically phenomenological, assuming timescale separations that often fail in regenerating tissues (Dieckmann and Law 1996; Dercole and Rinaldi 2008; Metz et al. 1995; Geritz et al. 1998). Without a rigorous derivation linking continuous micro-physics directly to macro-game competitive advantages, it remains unclear whether game-theoretic stability is a genuine biological property or a mathematical artifact. Recent work has connected stem–TD lineage dynamics across scales, from density-dependent continuous-time Markov chain models to diffusion approximations and aggregate total-mass laws, including ratio and equalization constraints in related damage-structured settings (Yu et al. 2026). The present work differs in deriving an exact deterministic closure and an induced game-theoretic interpretation directly from the transport model.

## 1.2 Contributions

In this work, we bridge this scale gap by deriving an exact closure of the total-mass balance laws into a planar ODE under uniform TD mortality. We move beyond metaphor to demonstrate that the “game” played by cells is an emergent physical property of lineage dynamics (Figure 1). Our specific contributions offer new theoretical and practical insights:

- (i) **Exact Dimensionality Reduction:** We identify a structural condition under which infinite-dimensional PDE dynamics collapse exactly into a two-variable system. We emphasize that this condition—uniform mortality among terminally differentiated (TD) cells—serves as a mathematical closure condition rather than

- a universal biological claim. It provides a rigorous justification for using simple compartment models to study complex, heterogeneous tissues.
- (ii) **Homeostasis as a Nash Equilibrium:** We establish that tissue homeostasis is mathematically equivalent to a Nash equilibrium in an induced evolutionary game. By deriving payoff functions” directly from cell-cycle parameters, we show stability is achieved when stem and TD phenotypes reach fitness equalization” (equal per-capita net growth rates).
  - (iii) **A Quantitative Extinction Threshold:** We establish a sharp “extinction-growth” threshold by analyzing the global phase-plane structure, proving that under compensatory feedback, the system globally converges to this homeostatic Nash equilibrium.
  - (iv) **Biological Validation (Murine Intestinal Crypts):** We apply these exact laws to a concrete, falsifiable case study of the murine intestinal crypt. The framework successfully models dedifferentiation-driven regeneration and provides a practical tool for biologists, allowing hard-to-measure rates (such as dedifferentiation flux) to be estimated directly from static, macroscopic flow cytometry observables.

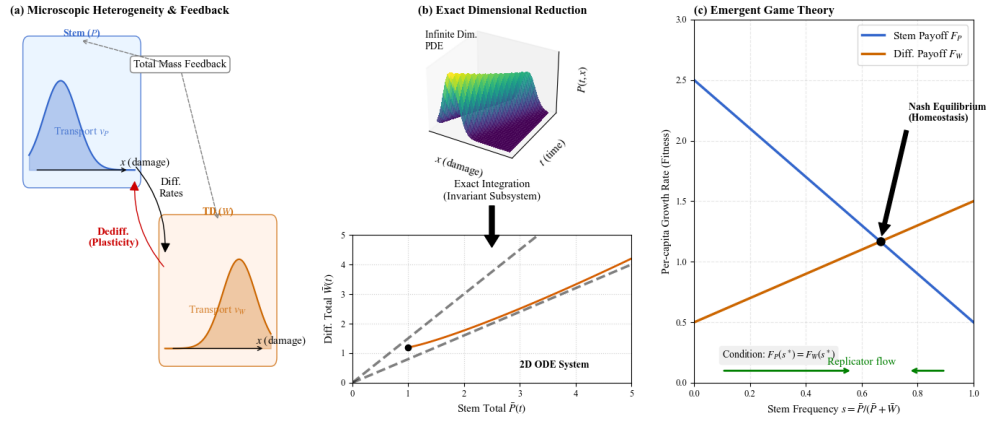


**Fig. 1 From microscopic heterogeneity to macroscopic game theory.** (a) **Microscopic scale:** Stem ( $P$ , blue) and TD ( $W$ , orange) cells are heterogeneous populations distributed over a damage coordinate  $x$ . (b) **Exact reduction:** The infinite-dimensional PDE dynamics (top surface) collapse exactly onto a 2D subsystem for totals (bottom phase plane) under uniform mortality. (c) **Macroscopic law:** Homeostasis emerges as a Nash equilibrium where per-capita growth rates (pay-offs) equalize. Green arrows indicate the replicator flow.

### 1.3 Most direct experimental settings and falsifiable readouts

The exact reduction and induced game structure are most directly testable in fast-renewing tissues where progenitor output is feedback-regulated and injury elicits measurable plasticity. Two canonical settings are rapidly renewing epithelia (e.g.,

intestinal crypts, airway epithelium) (Gall et al. 2023) and the hematopoietic system (Zhao and Baltimore 2015; Safina and Van Galen 2024).

In these paradigms, our theory makes three falsifiable predictions at the level of aggregate compartment readouts, testable via standard lineage tracing, pulse-chase, or EdU-BrdU proliferation assays. The framework is refuted if measured totals violate the closed balance laws under uniform mortality (Corollary 3.2; Fig. 3):

- (i) *Ratio Law and Equalization Law*: At steady state, the stem-to-TD ratio must satisfy  $\bar{P}^*/\bar{W}^* = \delta/\lambda_P(\bar{W}^*)$ . Similarly, the required dedifferentiation rate must match  $\lambda_R(\bar{P}^*) = \delta(p_2(\bar{W}^*) - p_1(\bar{W}^*))$ . Both quantities can be estimated from aggregate counts combined with division, death, and return-flux assays.
- (ii) *Nash Equilibrium*: The Nash/homeostasis condition is falsifiable as payoff equalization in observables. At the homeostatic point, both per-capita net growth rates vanish and coincide:  $F_P(\bar{P}^*, \bar{W}^*) = F_W(\bar{P}^*, \bar{W}^*) = 0$ .
- (iii) *Extinction–Growth Threshold*: This threshold is falsifiable through open-loop perturbations. Varying the renewal bias  $\Delta p = \hat{p}_1 - \hat{p}_2$  or the TD death rate  $\delta$  should switch the origin from stable (extinction) to saddle (growth) precisely at  $\Delta p_{\text{crit}} = -\hat{\lambda}_R/\delta$ .

The structure of the work goes as follows. Section 2 formulates the damage-structured PDE and establishes well-posedness. Section 3 derives exact balance laws and proves that under uniform mortality the infinite-dimensional dynamics close exactly to a two-dimensional ordinary differential equation (ODE). Section 4 identifies the induced replicator structure and shows homeostasis is a Nash equilibrium with closed-form game-theoretic laws. Section 5 establishes the extinction-growth threshold, proves global convergence via Bendixson–Dulac analysis, and rules out periodic orbits. Section 6 provides computational verification of all main results. Section 7 presents the case study on murine intestinal crypt homeostasis and regeneration. Section 8 discusses the experimental interpretation of our results and provides limitations and extensions of the present study.

## 2 Damage-structured PDE model

### 2.1 State variables and processes

We consider a two-compartment stem–TD lineage in which cells accumulate a scalar damage coordinate  $x \geq 0$ . Let  $P(t, x) \geq 0$  and  $W(t, x) \geq 0$  denote, respectively, the stem and TD densities at time  $t \geq 0$  and damage level  $x \geq 0$ . The corresponding total masses are

$$\bar{P}(t) = \int_0^\infty P(t, x) dx, \quad \bar{W}(t) = \int_0^\infty W(t, x) dx. \quad (1)$$

Damage accumulates deterministically along characteristics at constant speeds  $v_P, v_W > 0$ , yielding transport terms  $v_P \partial_x P$  and  $v_W \partial_x W$ , as in classical structured transport models (Perthame 2007, 2023). Stem cells divide with a feedback-regulated rate  $\lambda_P(\bar{W})$ , and upon division each daughter inherits a fixed fraction of the mother’s damage (deterministic inheritance). Concretely, a division event produces: (i) two stem

daughters with probability  $p_1(\bar{W})$  and damage fractions  $\alpha_1, \alpha_2 \in (0, 1)$ ; (ii) two TD daughters with probability  $p_2(\bar{W})$  and damage fractions  $\beta_1, \beta_2 \in (0, 1)$ ; (iii) one stem and one TD daughter with probability  $p_3(\bar{W}) := 1 - p_1(\bar{W}) - p_2(\bar{W})$  and damage fractions  $\gamma_1, \gamma_2 \in (0, 1)$ . Conservation at division imposes

$$\alpha_1 + \alpha_2 = \beta_1 + \beta_2 = \gamma_1 + \gamma_2 = 1. \quad (2)$$

The resulting nonlocal birth operators take the standard “push-forward” form induced by deterministic inheritance:

$$\begin{aligned} \mathcal{B}_P[P](t, x) &= \frac{p_1(\bar{W}(t))\lambda_P(\bar{W}(t))}{\alpha_1} P\left(t, \frac{x}{\alpha_1}\right) + \frac{p_1(\bar{W}(t))\lambda_P(\bar{W}(t))}{\alpha_2} P\left(t, \frac{x}{\alpha_2}\right) \\ &\quad + \frac{p_3(\bar{W}(t))\lambda_P(\bar{W}(t))}{\gamma_1} P\left(t, \frac{x}{\gamma_1}\right), \end{aligned} \quad (3)$$

$$\begin{aligned} \mathcal{B}_W[P](t, x) &= \frac{p_2(\bar{W}(t))\lambda_P(\bar{W}(t))}{\beta_1} P\left(t, \frac{x}{\beta_1}\right) + \frac{p_2(\bar{W}(t))\lambda_P(\bar{W}(t))}{\beta_2} P\left(t, \frac{x}{\beta_2}\right) \\ &\quad + \frac{p_3(\bar{W}(t))\lambda_P(\bar{W}(t))}{\gamma_2} P\left(t, \frac{x}{\gamma_2}\right). \end{aligned} \quad (4)$$

The concrete feedback functions  $\lambda_P$ ,  $\lambda_R$ , and  $p_i$  will appear in Section 2.2. In addition, TD cells can revert to the stem compartment via dedifferentiation  $W \rightarrow P$  with rate  $\lambda_R(\bar{P})$ , and TD cells die at a damage-dependent rate  $\delta(x) \geq 0$  (Section 2.2). Putting these components together yields the transport–reaction system (Wang et al. 2026)

$$\begin{cases} \partial_t P + v_P \partial_x P = \mathcal{B}_P[P](t, x) - \lambda_P(\bar{W}(t)) P(t, x) + \lambda_R(\bar{P}(t)) W(t, x), \\ \partial_t W + v_W \partial_x W = \mathcal{B}_W[P](t, x) - (\delta(x) + \lambda_R(\bar{P}(t))) W(t, x), \end{cases} \quad x > 0, t > 0. \quad (5)$$

Since  $v_P, v_W > 0$ , characteristics enter the domain at  $x = 0$ . We impose homogeneous inflow boundary conditions

$$P(t, 0) = W(t, 0) = 0, \quad t \geq 0, \quad (6)$$

so that newborn mass at small damage is generated by the nonlocal birth terms rather than injected through the boundary; this is consistent with standard structured-transport formulations and ensures boundary terms vanish in total-mass integrations (Perthame 2023; Liang et al. 2025). Initial data are prescribed by

$$P(0, x) = P_0(x), \quad W(0, x) = W_0(x), \quad x > 0. \quad (7)$$

## 2.2 Feedback maps and modeling assumptions

Numerous biological experiments have confirmed the existence of negative feedback regulators, where TD cells secrete signaling molecules to inhibit stem cell self-renewal

and proliferation. For instance, within the TGF- $\beta$  superfamily, GDF11 in the olfactory epithelium, GDF-8 (myostatin) in skeletal muscle, and BMP3 in bone act as critical molecular brakes that prevent hyperplasia by restricting progenitor expansion and tissue mass (Wu et al. 2003; McPherron et al. 1997; Daluiski et al. 2001). Furthermore, similar feedback loops are essential for stabilizing rapidly renewing tissues, such as the Cxcl12-mediated maintenance of hematopoietic stem cell quiescence and the autocrine TGF- $\beta$  mechanisms that limit keratinocyte overgrowth (Tzeng et al. 2011; Yamasaki et al. 2003).

At the same time, we consider the suppression of dedifferentiation by direct contact of TD cells with stem cells (Tata et al. 2013; Guo et al. 2022). Therefore, regulation is encoded through monotone (typically decreasing) Hill-type feedback maps,

$$\begin{aligned} p_1(\bar{W}) &= \frac{\hat{p}_1}{1 + (k_1\bar{W})^{m_1}}, & p_2(\bar{W}) &= \frac{\hat{p}_2}{1 + (k_2\bar{W})^{m_2}}, \\ \lambda_P(\bar{W}) &= \frac{\hat{\lambda}_P}{1 + (k_3\bar{W})^{m_3}}, & \lambda_R(\bar{P}) &= \frac{\hat{\lambda}_R}{1 + (k_4\bar{P})^{m_4}}, \end{aligned} \tag{8}$$

with gains  $k_i > 0$ , Hill exponents  $m_i \geq 1$ , and open-loop (baseline) values  $\hat{p}_i := p_i(0)$ ,  $\hat{\lambda}_P := \lambda_P(0)$ ,  $\hat{\lambda}_R := \lambda_R(0)$ .

We require  $p_1, p_2 \in [0, 1]$  and  $p_1(\bar{W}) + p_2(\bar{W}) \leq 1$  for all  $\bar{W} \geq 0$  so that  $p_3(\bar{W}) := 1 - p_1(\bar{W}) - p_2(\bar{W}) \in [0, 1]$ .

The TD death rate  $\delta(x)$  is assumed bounded and nonnegative. We distinguish two regimes:

- (i) **General bounded death**  $\delta(x)$ : used to establish global well-posedness and exact balance laws for totals (Theorem 3.1).
- (ii) **Uniform death**  $\delta(x) \equiv \delta$ : we consider the specific regime where environmental attrition dominates intrinsic mortality.

Uniform TD mortality is used here as a structural identifiability condition for exact closure, not as a claim that real tissues have perfectly damage-independent death. Exact closure on the two totals is guaranteed when  $\delta(x) \equiv \delta$ , because then the mortality flux reduces to  $\delta\bar{W}(t)$ . More generally, any regime in which the mortality flux depends only on  $\bar{W}(t)$  would also yield closure, but constant mortality is the canonical structurally identifiable case considered here. Therefore, the uniform mortality allows us to establish a baseline ‘neutral’ model against which age-dependent mortality can be compared. In that sense, “uniform death” is identifiable at the level of aggregate time series: failure of the closed balance laws is itself a diagnostic of non-uniform mortality. Figure 2 illustrates damage accumulation and inheritance mechanics and shows the feedback regulation for self-renewal and differentiation probabilities.

For the analysis below we adopt the following standing assumptions.

- Assumption 2.1.** (H1) The maps  $p_1, p_2, \lambda_P, \lambda_R$  are bounded and globally Lipschitz on  $[0, \infty)$  (e.g. the Hill families in (8) satisfy this).  
(H2)  $\delta \in L^\infty([0, \infty))$  is measurable and nonnegative.

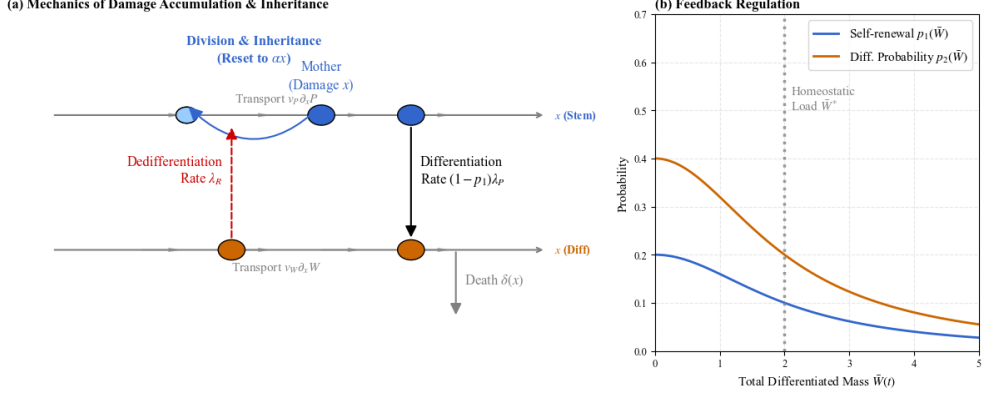


**Fig. 2 Mechanisms of damage dynamics and regulation.** (a) **Conveyor-belt dynamics:** Damage accumulates via transport (gray arrows). Division (blue arc) resets damage state ( $\alpha x < x$ ), while dedifferentiation (red) couples the compartments. (b) **Feedback logic:** Hill-type regulation of self-renewal ( $p_1$ ) and differentiation ( $p_2$ ) probabilities stabilizes the tissue burden  $\bar{W}$  at the homeostatic load  $\bar{W}^*$ .

$$(H3) \quad P_0, W_0 \in L^1_+([0, \infty)).$$

### 2.3 Well-posedness setting and weak/mild solutions

Fix  $T > 0$  and define the state space

$$\mathcal{X}_T := C([0, T]; L^1([0, \infty)) \times L^1([0, \infty))), \quad \|(P, W)\|_{\mathcal{X}_T} := \sup_{t \in [0, T]} (\|P(t, \cdot)\|_1 + \|W(t, \cdot)\|_1), \quad (9)$$

with  $\|\cdot\|_1 = \|\cdot\|_{L^1([0, \infty))}$ . Under Assumption 2.1, system (5) can be formulated in mild form along characteristics. Let

$$X_P(s; t, x) = x - v_P(t - s), \quad X_W(s; t, x) = x - v_W(t - s), \quad 0 \leq s \leq t,$$

and define integrating factors

$$\Lambda_P(s; t) = \int_s^t \lambda_P(\bar{W}(\tau)) d\tau, \quad \Lambda_W(s; t, x) = \int_s^t (\delta(X_W(\tau; t, x)) + \lambda_R(\bar{P}(\tau))) d\tau.$$

A mild solution  $(P, W) \in \mathcal{X}_T$  is then a fixed point of the Picard map obtained by inserting (3) into the characteristic representations (cf. standard semigroup/characteristic constructions for transport equations with inflow boundary conditions (Perthame 2023)). The global Lipschitz property in (H1) yields a contraction for small  $T$ ; positivity is preserved by the nonnegativity of kernels and rates; and an a priori  $L^1$ -mass bound provides continuation to all times. We therefore obtain a unique global non-negative solution in  $\mathcal{X}_\infty := C([0, \infty); L^1 \times L^1)$ , together with exact balance laws for  $\bar{P}$  and  $\bar{W}$  (Theorem 3.1).

### 3 Balance laws and exact reduction

#### 3.1 Balance laws for totals (general $\delta(x)$ )

We first derive exact balance laws for the total masses  $\bar{P}(t)$  and  $\bar{W}(t)$  defined in (1), under a general bounded, nonnegative death profile  $\delta(x)$ .

**Theorem 3.1** (Balance laws for totals) *Assume Assumption 2.1. Then the PDE system (5)–(7) admits a unique global nonnegative solution  $(P, W) \in C([0, \infty); L^1([0, \infty)) \times L^1([0, \infty)))$ . Moreover, the total masses satisfy, for a.e.  $t > 0$ ,*

$$\begin{cases} \frac{d\bar{P}}{dt} = (p_1(\bar{W}) - p_2(\bar{W}))\lambda_P(\bar{W})\bar{P} + \lambda_R(\bar{P})\bar{W}, \\ \frac{d\bar{W}}{dt} = (1 - p_1(\bar{W}) + p_2(\bar{W}))\lambda_P(\bar{W})\bar{P} - \lambda_R(\bar{P})\bar{W} - \int_0^\infty \delta(x)W(t, x) dx, \end{cases} \quad (10)$$

with initial conditions  $\bar{P}(0) = \|P_0\|_1$  and  $\bar{W}(0) = \|W_0\|_1$ .

*Proof sketch (derivation of (10))* We outline the formal computation; the rigorous argument follows by testing the weak formulation against cutoffs  $\psi_R(x)$  and passing  $R \rightarrow \infty$ , where  $\psi_R \equiv 1$  on  $[0, R]$ ,  $\text{supp } \psi_R \subset [0, R + 1]$  and  $\|\psi'_R\|_\infty \leq C$  with  $C$  independent of  $R$  (cf. standard transport weak formulations).

Integrate the  $P$ -equation in (5) over  $x \in (0, \infty)$ :

$$\frac{d}{dt} \int_0^\infty P dx + \int_0^\infty v_P \partial_x P dx = \int_0^\infty \mathcal{B}_P[P] dx - \lambda_P(\bar{W}) \int_0^\infty P dx + \lambda_R(\bar{P}) \int_0^\infty W dx.$$

The transport term gives the boundary flux  $\int_0^\infty v_P \partial_x P dx = v_P P(t, \infty) - v_P P(t, 0)$ . Under integrability and the inflow boundary condition (6), this term vanishes:  $P(t, \infty) = 0$  (in the sense of  $L^1$  tails) and  $P(t, 0) = 0$  (in the sense of traces for  $L^1$  solutions to transport equations). An identical computation holds for the  $W$ -equation.

It remains to compute  $\int \mathcal{B}_P[P] dx$  and  $\int \mathcal{B}_W[P] dx$ . Using the change of variables  $y = x/\alpha$ ,

$$\int_0^\infty \frac{1}{\alpha} P\left(t, \frac{x}{\alpha}\right) dx = \int_0^\infty P(t, y) dy = \bar{P}(t),$$

and similarly for  $\alpha \in \{\alpha_i, \beta_i, \gamma_i\}$ , together with  $p_1 + p_2 + p_3 = 1$ , one obtains

$$\begin{aligned} \int_0^\infty \mathcal{B}_P[P] dx &= (2p_1(\bar{W}) + p_3(\bar{W}))\lambda_P(\bar{W})\bar{P} = (1 + p_1(\bar{W}) - p_2(\bar{W}))\lambda_P(\bar{W})\bar{P}, \\ \int_0^\infty \mathcal{B}_W[P] dx &= (2p_2(\bar{W}) + p_3(\bar{W}))\lambda_P(\bar{W})\bar{P} = (1 - p_1(\bar{W}) + p_2(\bar{W}))\lambda_P(\bar{W})\bar{P}. \end{aligned}$$

Substituting these identities yields (10).  $\square$

#### **Why the inflow boundary removes flux terms**

Because  $v_P, v_W > 0$ , characteristics enter the half-line through  $x = 0$  (an inflow boundary). The condition (6) enforces zero boundary trace at  $x = 0$ , so the integrated transport flux produces no boundary contribution in the balance laws (after justification via cutoff testing and  $R \rightarrow \infty$ ).

### 3.2 Exact two-dimensional closure under uniform death

The balance laws (10) are not closed in general, because the mortality term depends on the *distribution*  $W(t, \cdot)$  through  $\int_0^\infty \delta(x)W(t, x) dx$ . A key structural simplification occurs when the TD death rate is constant.

**Corollary 3.2** (Exact two-compartment closure for  $\delta(x) \equiv \delta$ ) *If  $\delta(x) \equiv \delta > 0$  is constant, then  $\int_0^\infty \delta(x)W(t, x) dx = \delta \bar{W}(t)$  and the balance laws close exactly to the planar ODE system*

$$\begin{cases} \dot{\bar{P}} = \left( p_1(\bar{W}) - p_2(\bar{W}) \right) \lambda_P(\bar{W}) \bar{P} + \lambda_R(\bar{P}) \bar{W}, \\ \dot{\bar{W}} = \left( 1 - p_1(\bar{W}) + p_2(\bar{W}) \right) \lambda_P(\bar{W}) \bar{P} - (\delta + \lambda_R(\bar{P})) \bar{W}, \end{cases} \quad (11)$$

$$(\bar{P}(0), \bar{W}(0)) = (\|P_0\|_1, \|W_0\|_1).$$

The closed quadrant  $\{\bar{P} \geq 0, \bar{W} \geq 0\}$  is forward invariant, and solutions are global.

*Proof sketch* Closure is immediate from  $\int_0^\infty \delta W dx = \delta \bar{W}$ . Forward invariance follows from evaluating the vector field on the boundary: if  $\bar{P} = 0$  and  $\bar{W} \geq 0$ , then  $\dot{\bar{P}} = \lambda_R(0)\bar{W} \geq 0$ ; if  $\bar{W} = 0$  and  $\bar{P} \geq 0$ , then  $\dot{\bar{W}} = (1 - p_1(0) + p_2(0))\lambda_P(0)\bar{P} \geq 0$ . For global existence, set  $M(t) := \bar{P}(t) + \bar{W}(t)$  and compute from (11)

$$\dot{M}(t) = \lambda_P(\bar{W}(t)) \bar{P}(t) - \delta \bar{W}(t) \leq \hat{\lambda}_P M(t), \quad (12)$$

where  $\hat{\lambda}_P = \lambda_P(0)$  and we used  $\lambda_P(\cdot) \leq \hat{\lambda}_P$  and  $\bar{P} \leq M$ . Gronwall's inequality yields  $M(t) \leq M(0)e^{\hat{\lambda}_P t}$  for all  $t \geq 0$ , precluding finite-time blow-up and implying global existence.  $\square$

### 3.3 What breaks when $\delta(x)$ is non-constant

When  $\delta(x)$  varies with damage, the mortality term in (10) becomes

$$\int_0^\infty \delta(x) W(t, x) dx,$$

which depends on the full distribution  $W(t, \cdot)$  rather than the single scalar  $\bar{W}(t)$ . Consequently, the pair  $(\bar{P}, \bar{W})$  does not form a closed dynamical system in general: additional moments (e.g.  $\int \delta(x)W dx$ , or other weighted integrals) are required, and any finite-dimensional closure would typically be approximate. Such approximate closures are common in hybrid and stochastic multiscale models, where deterministic mean-field limits are obtained by closing higher-order correlations (e.g. first-moment closure) to yield tractable PDE surrogates (Wang et al. 2025). Figure 3 compares the uniform death rate and variable death rate scenarios. It provides the mechanistic contrast: when  $\delta(x) \equiv \delta$ , mortality depends only on total mass and the PDE totals obey the closed ODE exactly; when  $\delta(x)$  varies with damage, the mortality flux depends on the shape of  $W(t, \cdot)$ , breaking closure and requiring additional moments.

*Remark 3.3* (Uniform death as an identifiability/closure condition (not a biological claim)). The specialization  $\delta(x) \equiv \delta$  should be read as a structural identifiability condition for exact closure, not as a literal assertion that TD mortality is

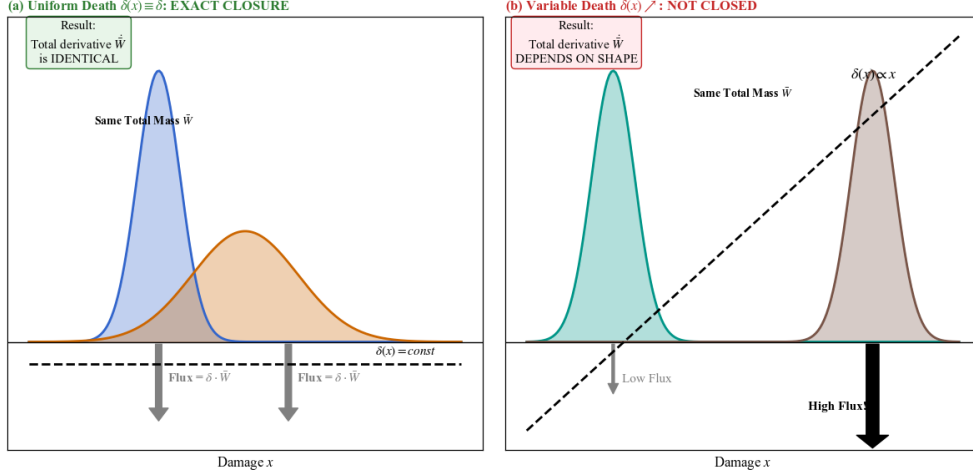


**Fig. 3 Why uniform mortality enables exact dimensional reduction. (a) Uniform death ( $\delta(x) \equiv \delta$ ):** Mortality flux depends only on total mass (area), ensuring exact closure regardless of distribution shape. **(b) Variable death ( $\delta(x) \nearrow$ ):** Mortality flux depends on the distribution's shape (e.g., age structure), breaking the ODE closure. This figure also serves as the mechanistic counterfactual: any observed deviation of total-mass trajectories from (11) (beyond numerical error) indicates a non-constant effective mortality and hence failure of exact closure.

damage-independent in vivo. The balance laws in Theorem 3.1 show that the only obstruction to a closed two-dimensional dynamics on totals  $(\bar{P}, \bar{W})$  is the mortality flux  $\int_0^\infty \delta(x)W(t, x) dx$ . Exact closure on  $(\bar{P}, \bar{W})$  occurs precisely when this flux can be written as a function of  $\bar{W}(t)$  alone, i.e. when  $\int_0^\infty \delta(x)W(t, x) dx = \delta \bar{W}(t)$ , yielding the planar ODE system in Corollary 3.2. Conversely, when  $\delta(x)$  varies with damage, the flux depends on the shape of  $W(t, \cdot)$  rather than its total mass, breaking the reduction (Fig.3) and implying that any low-dimensional closure must include additional distributional information (e.g. weighted moments). Importantly, this condition is identifiable at the level of totals: if aggregate trajectories  $(\bar{P}(t), \bar{W}(t))$  fail to satisfy the closed balance laws (11) beyond discretization error (Section 6.4, Fig. 7), then the uniform-death closure is empirically falsified for that regime.

This observation motivates the uniform-death assumption  $\delta(x) \equiv \delta$  as a structural hypothesis under which the PDE-to-ODE reduction is exact and analytically tractable. Importantly, uniform death is also identifiable at the level of totals: it is precisely the condition under which the mortality flux can be written as  $\delta \bar{W}(t)$ , yielding a closed two-dimensional system whose equilibrium laws and global dynamics can be tested against time-series measurements of aggregate stem/TD abundances.

## 4 Replicator mapping and game-theoretic interpretation

In this section we show that the exact two-compartment closure obtained under uniform TD death (Corollary 3.2) induces a replicator-type frequency dynamics. This provides an organizing interpretation in which strategies correspond to phenotypes (stem vs. TD), and payoffs are the phenotypes' per-capita net growth rates. Importantly, the game-theoretic structure here is not postulated: it is derived mechanistically from the PDE bookkeeping via the exact reduction. The induced game is state dependent: the “payoffs” are not constants from a payoff matrix, but per-capita growth rates generated by the underlying feedback-regulated lineage dynamics. Replicator dynamics are standard in evolutionary game theory and population dynamics (Schuster and Sigmund 1983; Hofbauer and Sigmund 1998; Cressman and Tao 2014).

### 4.1 Frequency dynamics

Assume  $\delta(x) \equiv \delta > 0$  so that the totals  $(\bar{P}, \bar{W})$  satisfy the closed ODE system (11) on the forward-invariant quadrant  $\bar{P}, \bar{W} \geq 0$ . For interior states  $\bar{P}, \bar{W} > 0$ , define the per-capita net growth rates

$$F_P(\bar{P}, \bar{W}) := \frac{\dot{\bar{P}}}{\bar{P}}, \quad F_W(\bar{P}, \bar{W}) := \frac{\dot{\bar{W}}}{\bar{W}}. \quad (13)$$

These quantities play the role of state-dependent payoffs in the induced two-strategy game.

Let  $M(t) := \bar{P}(t) + \bar{W}(t)$  denote the total mass and define the stem frequency

$$s(t) := \frac{\bar{P}(t)}{M(t)} \in (0, 1), \quad 1 - s(t) = \frac{\bar{W}(t)}{M(t)}. \quad (14)$$

A direct computation yields the replicator form

$$\dot{s} = \frac{\dot{\bar{P}}}{M} - \frac{\bar{P}}{M^2} \dot{M} = \frac{\bar{P}}{M} \left(1 - \frac{\bar{P}}{M}\right) \left(\frac{\dot{\bar{P}}}{\bar{P}} - \frac{\dot{\bar{W}}}{\bar{W}}\right) = s(1-s)(F_P - F_W), \quad (15)$$

which is the familiar two-strategy replicator equation with payoffs given by per-capita growth (Hofbauer and Sigmund 1998; Cressman and Tao 2014). Equation (15) shows that the sign of  $F_P - F_W$  determines the direction of selection on stemness: if stem cells have higher per-capita net growth ( $F_P > F_W$ ), then  $s$  increases; otherwise  $s$  decreases.

### 4.2 Nash/homeostasis equivalence

For two-strategy replicator dynamics, interior rest points correspond to payoff equalization across strategies in support (Hofbauer and Sigmund 1998). In our setting this equalization has a concrete biological meaning: at homeostasis, stem and TD phenotypes have identical per-capita net growth, so neither phenotype has a selective

advantage in the aggregated (well-mixed) dynamics. In (13), we interpret  $F_P, F_W$  as state-dependent payoffs of an induced two-strategy game.

**Theorem 4.1** (Interior equilibrium  $\iff$  payoff equalization) *Assume  $\delta(x) \equiv \delta > 0$  and let  $(\bar{P}, \bar{W}) \in (0, \infty)^2$ . Then,*

(i)  $(\bar{P}, \bar{W})$  is an equilibrium if and only if the per-capita rates are equal and the common per-capita rate vanishes; equivalently,

$$(\bar{P}, \bar{W}) \text{ is an equilibrium} \iff F_P(\bar{P}, \bar{W}) = F_W(\bar{P}, \bar{W}) = 0.$$

(ii) Separately,  $F_P = F_W$  (on an interior state) is equivalent to the frequency  $s = \bar{P}/(\bar{P} + \bar{W})$  being a rest point of the replicator equation  $\dot{s} = s(1-s)(F_P - F_W)$ .

*Proof* (i) If  $(\bar{P}, \bar{W})$  is an equilibrium then  $\dot{\bar{P}} = \dot{\bar{W}} = 0$ . By the definitions

$$F_P(\bar{P}, \bar{W}) = \frac{\dot{\bar{P}}}{\bar{P}}, \quad F_W(\bar{P}, \bar{W}) = \frac{\dot{\bar{W}}}{\bar{W}},$$

we obtain  $F_P(\bar{P}, \bar{W}) = F_W(\bar{P}, \bar{W}) = 0$ .

Conversely, if  $F_P(\bar{P}, \bar{W}) = F_W(\bar{P}, \bar{W}) = 0$  then  $\dot{\bar{P}} = F_P \bar{P} = 0$  and  $\dot{\bar{W}} = F_W \bar{W} = 0$ , so  $(\bar{P}, \bar{W})$  is an equilibrium. (We remark that  $F_P = F_W$  alone only implies the existence of a common per-capita rate  $c$  with  $\dot{\bar{P}} = c\bar{P}$ ,  $\dot{\bar{W}} = c\bar{W}$ , and the additional requirement  $c = 0$  is necessary for a fixed point.)

(ii) Let  $M = \bar{P} + \bar{W}$  and  $s = \bar{P}/M$ . By (15), on the interior  $s \in (0, 1)$  we have  $\dot{s} = 0$  if and only if  $F_P = F_W$ , as claimed.  $\square$

In evolutionary game theory, a mixed Nash equilibrium equalizes the expected payoffs of strategies in its support; otherwise a player could unilaterally switch to a higher-payoff strategy (Hofbauer and Sigmund 1998). Theorem 4.1 shows that in our model, homeostasis is exactly such a payoff equalization condition, with payoffs derived from the mechanistic division–differentiation–dedifferentiation–death bookkeeping.

### 4.3 Closed-form laws and experimental observables

A key advantage of the present reduction is that payoff equalization can be rewritten as explicit algebraic identities among measurable quantities. Under uniform death, the interior equilibrium relations can be expressed in closed form.

**Theorem 4.2** (Homeostatic laws under uniform death) *Assume  $\delta(x) \equiv \delta > 0$ . An interior equilibrium  $(\bar{P}^*, \bar{W}^*) \in (0, \infty)^2$  of (11) exists if and only if the following identities hold:*

$$(p_2(\bar{W}^*) - p_1(\bar{W}^*)) \delta = \lambda_R(\bar{P}^*), \quad (\text{Equalization law}) \quad (16)$$

$$\frac{\bar{P}^*}{\bar{W}^*} = \frac{\delta}{\lambda_P(\bar{W}^*)}. \quad (\text{Ratio law}) \quad (17)$$

At such an equilibrium,  $F_P(\bar{P}^*, \bar{W}^*) = F_W(\bar{P}^*, \bar{W}^*)$  (payoff equalization), and the induced frequency  $s^* = \bar{P}^*/(\bar{P}^* + \bar{W}^*)$  is a rest point of (15).

*Proof* At equilibrium,  $\dot{P} = \dot{W} = 0$  in (11). From  $\dot{P} = 0$ ,

$$\lambda_R(\bar{P}^*) \bar{W}^* = (p_2(\bar{W}^*) - p_1(\bar{W}^*)) \lambda_P(\bar{W}^*) \bar{P}^*.$$

From  $\dot{W} = 0$ ,

$$(\delta + \lambda_R(\bar{P}^*)) \bar{W}^* = (1 - p_1(\bar{W}^*) + p_2(\bar{W}^*)) \lambda_P(\bar{W}^*) \bar{P}^*.$$

Dividing the second identity by the first yields (16); substituting back gives (17). The remaining statements follow from Theorem 4.1.  $\square$

Figure 4 illustrates the geometry of the homeostasis state, including the Nash equilibrium  $(\bar{P}^*, \bar{W}^*)$  as the intersection of the Ratio law and the Equalization law (Theorem 4.2), and the replicator dynamics with respect to the stem frequency  $s$ .

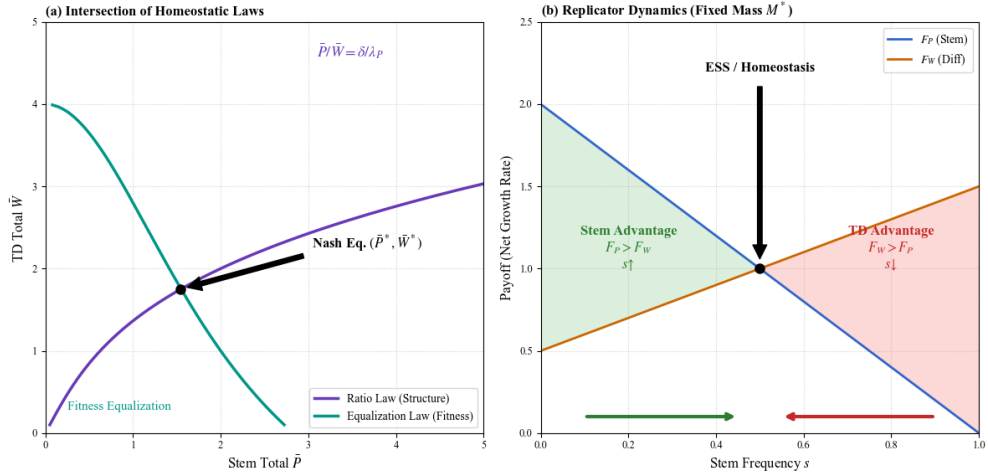


**Fig. 4 The geometry of homeostasis.** (a) **Intersection of laws:** The unique Nash equilibrium is determined by the intersection of the Ratio Law (purple) and Equalization Law (teal) curves. (b) **Replicator stability:** The Nash point is a stable interior rest point of the induced replicator dynamics in the parameter regime shown. Green/red zones indicate regions where stem/TD phenotypes have a fitness advantage ( $F_P > F_W$  or  $F_W > F_P$ ), driving the frequency  $s$  toward equilibrium.

Equations (16)–(17) are algebraic relations among aggregate observables and effective rates at homeostasis:

- (i)  $\bar{P}^*$  and  $\bar{W}^*$  are steady-state compartment sizes, measurable by cell counting, flow cytometry, or lineage-marker gating (stem vs. TD markers) (Vadakke-Madathil et al. 2019; Bose et al. 2023).
- (ii)  $\delta$  is the TD death rate; in steady conditions it can be estimated by apoptosis/necrosis assays (e.g. Annexin V/PI) or survival analysis of labeled TD cohorts (Crowley et al. 2016; Chen 2009).

- (iii)  $\lambda_P(\bar{W}^*)$  is the effective stem division rate at TD load  $\bar{W}^*$ ; it can be estimated from proliferation readouts (EdU/BrdU incorporation, mitotic index, or time-lapse lineage tracking) conditioned on the observed steady  $\bar{W}^*$  (Huelsz-Prince et al. 2022).
- (iv)  $\lambda_R(\bar{P}^*)$  is the effective dedifferentiation rate at stem load  $\bar{P}^*$ ; it can be inferred from lineage tracing that quantify TD  $\rightarrow$  stem return flux under steady-state conditions (Weinberg et al. 2007).

Thus, the equalization and Ratio laws provide directly testable predictions: once  $\delta$  and  $\lambda_P(\bar{W}^*)$  are estimated, the steady-state ratio  $\bar{P}^*/\bar{W}^*$  is predicted by (17), and the dedifferentiation rate required to offset net differentiation losses is predicted by (16).

## 5 Dynamics: thresholds, uniqueness, and global stability

Throughout this section we assume the uniform TD death regime  $\delta(x) \equiv \delta > 0$ , so that the PDE balance laws close exactly to the planar ODE system on totals  $(\bar{P}, \bar{W})$  (Corollary 3.2):

$$\begin{cases} \dot{\bar{P}} = (p_1(\bar{W}) - p_2(\bar{W}))\lambda_P(\bar{W})\bar{P} + \lambda_R(\bar{P})\bar{W}, \\ \dot{\bar{W}} = (1 - p_1(\bar{W}) + p_2(\bar{W}))\lambda_P(\bar{W})\bar{P} - (\delta + \lambda_R(\bar{P}))\bar{W}. \end{cases} \quad (18)$$

The closed quadrant  $\{\bar{P} \geq 0, \bar{W} \geq 0\}$  is forward invariant and solutions are global (Corollary 3.2). Our aim is to expose the global qualitative structure: a structural threshold at extinction, uniqueness of the interior equilibrium via a one-dimensional reduction, and global non-oscillatory convergence under compensatory feedback.

### 5.1 Extinction–growth threshold at the origin

We analyze the extinction state  $(\bar{P}, \bar{W}) = (0, 0)$  by open-loop linearization. Let

$$\hat{p}_i := p_i(0), \quad \hat{\lambda}_P := \lambda_P(0), \quad \hat{\lambda}_R := \lambda_R(0), \quad \Delta p := \hat{p}_1 - \hat{p}_2.$$

Then the Jacobian of (18) at the origin is

$$A(\Delta p) = \begin{pmatrix} \Delta p \hat{\lambda}_P & \hat{\lambda}_R \\ (1 - \Delta p) \hat{\lambda}_P & -(\delta + \hat{\lambda}_R) \end{pmatrix}, \quad (19)$$

with trace and determinant

$$\text{tr } A(\Delta p) = \Delta p \hat{\lambda}_P - (\delta + \hat{\lambda}_R), \quad \det A(\Delta p) = -\delta \hat{\lambda}_P \left( \Delta p + \frac{\hat{\lambda}_R}{\delta} \right). \quad (20)$$

**Theorem 5.1** (Structural extinction–growth threshold) *Define*

$$\Delta p_{\text{crit}} = -\frac{\hat{\lambda}_R}{\delta}. \quad (21)$$

*Then:*

- (i) *If  $\Delta p < \Delta p_{\text{crit}}$ , then  $\det A > 0$  and  $\text{tr } A < 0$ , hence the origin is locally asymptotically stable (extinction regime).*
- (ii) *If  $\Delta p = \Delta p_{\text{crit}}$ , then  $\det A = 0$  and one eigenvalue is 0 (threshold case).*
- (iii) *If  $\Delta p > \Delta p_{\text{crit}}$ , then  $\det A < 0$ , hence the origin is a saddle with a one-dimensional unstable manifold (growth regime).*

*Proof* The transition occurs when  $\det A(\Delta p) = 0$ , i.e.  $\Delta p = -\hat{\lambda}_R/\delta$  by (20). The sign patterns in (20) give the classification.  $\square$

Equation (21) is a structural threshold: it depends only on (i) uniform death  $\delta$ , and (ii) open-loop renewal–differentiation mismatch  $\Delta p$ , and it follows from the sign change of  $\det A$ . This makes (21) robust to the detailed shape of feedback maps, and directly interpretable as the dividing line between washout/extinction and departure from extinction. Explicit feedback-controlled thresholds are also a recurring outcome in other coupled continuum/hybrid systems, e.g., finite-domain instability thresholds in bidirectionally coupled endothelial–factor dynamics (Liu et al. 2025).

## 5.2 Uniqueness of the interior equilibrium via a one-dimensional reduction

At any interior equilibrium  $(\bar{P}^*, \bar{W}^*) \in (0, \infty)^2$ , the closed-form laws from Section 4.3 hold:

$$\lambda_R(\bar{P}^*) = (p_2(\bar{W}^*) - p_1(\bar{W}^*))\delta, \quad \frac{\bar{P}^*}{\bar{W}^*} = \frac{\delta}{\lambda_P(\bar{W}^*)}. \quad (22)$$

The Ratio law defines the *ratio curve*

$$\bar{P} = \bar{P}(\bar{W}) := \frac{\delta}{\lambda_P(\bar{W})} \bar{W}, \quad \bar{W} > 0. \quad (23)$$

Substituting (23) into the Equalization law yields a scalar root condition.

**One-dimensional residual.** Assume  $\lambda_R$  is strictly decreasing (hence invertible on its range) and define

$$G(\bar{W}) := \lambda_R^{-1}\left(\delta(p_2(\bar{W}) - p_1(\bar{W}))\right) - \frac{\delta}{\lambda_P(\bar{W})} \bar{W}, \quad \bar{W} > 0. \quad (24)$$

Then  $\bar{W}^* > 0$  solves  $G(\bar{W}^*) = 0$  if and only if  $\bar{P}^* = \bar{P}(\bar{W}^*)$  and  $(\bar{P}^*, \bar{W}^*)$  is an interior equilibrium of (18).

**Theorem 5.2** (Uniqueness under a verifiable slope condition) *Assume  $p_1, p_2, \lambda_P \in C^1([0, \infty))$  with  $\lambda_P(\bar{W}) > 0$  and  $\lambda'_P(\bar{W}) < 0$ , and  $\lambda_R \in C^1([0, \infty))$  with  $\lambda'_R(\bar{P}) < 0$ . Define  $\Delta(\bar{W}) := p_2(\bar{W}) - p_1(\bar{W})$  and  $\bar{P}(\bar{W})$  by (23). Suppose  $\Delta(\bar{W}) \geq 0$  for  $\bar{W} \geq 0$  and  $\Delta'(\bar{W}) < 0$  on the relevant range. If the slope dominance condition*

$$-\lambda'_R(\bar{P}(\bar{W})) \bar{P}'(\bar{W}) < -\delta \Delta'(\bar{W}) \quad \text{for all } \bar{W} > 0 \quad (25)$$

holds, then the function

$$r(\bar{W}) := \delta \Delta(\bar{W}) - \lambda_R(\bar{P}(\bar{W})) \quad (26)$$

is strictly decreasing on  $(0, \infty)$  and has at most one root. Consequently, (18) admits at most one interior equilibrium.

*Proof* Differentiate (26) using the chain rule:

$$r'(\bar{W}) = \delta \Delta'(\bar{W}) - \lambda'_R(\bar{P}(\bar{W})) \bar{P}'(\bar{W}).$$

Under (25),  $r'(\bar{W}) < 0$  for all  $\bar{W} > 0$ , hence  $r$  is strictly decreasing and can cross 0 at most once. Finally,  $r(\bar{W}) = 0$  is equivalent to the equalization law evaluated on the ratio curve (23), hence to interior equilibria.  $\square$

### Computable form of (25)

From (23),

$$\bar{P}'(\bar{W}) = \delta \frac{\lambda_P(\bar{W}) - \bar{W} \lambda'_P(\bar{W})}{\lambda_P(\bar{W})^2} > 0 \quad (\text{since } \lambda_P > 0, \lambda'_P < 0). \quad (27)$$

Thus (25) compares a dedifferentiation sensitivity term  $-\lambda'_R(\bar{P}) \bar{P}'(\bar{W})$  against a differentiation-gap sensitivity term  $-\delta \Delta'(\bar{W})$ , and can be checked numerically for any given feedback parameterization (e.g. Hill families).

### A weaker (nontriviality) uniqueness statement

Even without (25), if at least one of  $\Delta(\cdot)$  or  $\lambda_R(\cdot)$  is non-constant and strictly monotone, then the pair of algebraic laws (22) generically determines at most one interior equilibrium (cf. the one-dimensional solver in Section 6), and Theorem 5.2 provides a clean, verifiable sufficient condition.

## 5.3 Compensatory feedback and non-oscillation (global structure)

We now identify a sign/monotonicity regime enforcing global non-oscillatory dynamics in the interior of the quadrant.

**Definition 5.3** (Compensatory feedback). We say the feedback is *compensatory* if

- (i)  $p'_1(\bar{W}) > p'_2(\bar{W})$  for all  $\bar{W} \geq 0$  (in particular  $p'_1, p'_2 < 0$ ), equivalently  $\Delta'(\bar{W}) = p'_2(\bar{W}) - p'_1(\bar{W}) < 0$ ;
- (ii)  $p_1(\bar{W}) < p_2(\bar{W})$  on the relevant range, equivalently  $\Delta(\bar{W}) > 0$ .

**Theorem 5.4** (Negative divergence and exclusion of periodic orbits) *Assume  $\delta > 0$  is constant and that  $p_1, p_2, \lambda_P$  are  $C^1$ , bounded, strictly decreasing in  $\bar{W}$ , while  $\lambda_R$  is  $C^1$ , bounded, strictly decreasing in  $\bar{P}$ . If Definition 5.3 holds, then the divergence of the vector field  $\mathbf{G} = (G_1, G_2)$  in (18) satisfies*

$$\nabla \cdot \mathbf{G}(\bar{P}, \bar{W}) = \partial_{\bar{P}} G_1(\bar{P}, \bar{W}) + \partial_{\bar{W}} G_2(\bar{P}, \bar{W}) < 0 \quad \forall (\bar{P}, \bar{W}) \in (0, \infty)^2. \quad (28)$$

Consequently, by the Bendixson–Dulac criterion (take Dulac function  $\varphi \equiv 1$ ), (18) admits no nontrivial periodic orbit contained in  $(0, \infty)^2$ .

*Proof* Compute

$$\partial_{\bar{P}} G_1(\bar{P}, \bar{W}) = (p_1(\bar{W}) - p_2(\bar{W})) \lambda_P(\bar{W}) + \lambda'_R(\bar{P}) \bar{W} < 0$$

since  $p_1 - p_2 < 0$  and  $\lambda'_R < 0$ . Next,

$$\partial_{\bar{W}} G_2(\bar{P}, \bar{W}) = \left[ (-p'_1(\bar{W}) + p'_2(\bar{W})) \lambda_P(\bar{W}) + (1 - p_1(\bar{W}) + p_2(\bar{W})) \lambda'_P(\bar{W}) \right] \bar{P} - (\delta + \lambda_R(\bar{P})).$$

Under compensatory feedback,  $-p'_1 + p'_2 = \Delta'(\bar{W}) < 0$ ; moreover  $\lambda'_P(\bar{W}) < 0$  and  $1 - p_1 + p_2 > 0$ , hence the bracketed term is negative, so  $\partial_{\bar{W}} G_2 < 0$ . Summing yields (28). The Bendixson–Dulac criterion (Perko 2001) applies on any simply connected subset of  $(0, \infty)^2$  to exclude periodic orbits.  $\square$

**Theorem 5.5** (Global convergence among bounded trajectories) *Assume the hypotheses of Theorem 5.4. If an interior equilibrium exists and is unique (e.g. by Theorem 5.2), then every bounded trajectory of (18) with initial data in  $(0, \infty)^2$  converges to that equilibrium as  $t \rightarrow \infty$ .*

*Proof* Let  $(\bar{P}(t), \bar{W}(t))$  be a bounded trajectory in  $(0, \infty)^2$ . Its  $\omega$ -limit set is nonempty, compact, and invariant. By the Poincaré–Bendixson theorem, the  $\omega$ -limit set is either an equilibrium, a periodic orbit, or a union of equilibria with connecting orbits. Theorem 5.4 excludes periodic orbits, hence the  $\omega$ -limit set consists of equilibria (possibly with heteroclinic connections). Uniqueness of the interior equilibrium forces the  $\omega$ -limit set to be that single point, i.e. convergence.  $\square$

### **Global structure (not merely local stability)**

Theorems 5.4–5.5 constrain the entire phase portrait in the interior: oscillations are ruled out and bounded dynamics must settle to equilibrium. This is strictly stronger than a local eigenvalue computation at  $(\bar{P}^*, \bar{W}^*)$ .

## **5.4 Scaling invariance under uniform gain amplification**

Finally, the Hill feedback family (8) admits a scaling symmetry that separates composition from scale. For  $A > 0$ , rescale all Hill gains by  $k_i \mapsto Ak_i$  and denote the corresponding maps by  $p_{j,A}, \lambda_{P,A}, \lambda_{R,A}$ . Then  $p_{j,A}(w/A) = p_j(w)$  and  $\lambda_{P,A}(w/A) = \lambda_P(w)$ , while  $\lambda_{R,A}(p/A) = \lambda_R(p)$ .

**Proposition 5.6** (Gain-scaling symmetry) *Assume uniform death  $\delta > 0$  and Hill-type feedback (8). If  $(\bar{P}^*, \bar{W}^*)$  is an interior equilibrium of (18), then*

$$(\bar{P}^*, \bar{W}^*) \mapsto \left( \frac{\bar{P}^*}{A}, \frac{\bar{W}^*}{A} \right) \quad (29)$$

*is an interior equilibrium of the gain-scaled system. Moreover, the equilibrium ratio  $\bar{P}^*/\bar{W}^*$  is invariant under this transformation.*

*Proof sketch* The equilibrium is characterized by the two algebraic laws (16)–(17). Under the gain scaling, evaluating the scaled maps at  $(\bar{P}^*/A, \bar{W}^*/A)$  reproduces the original values at  $(\bar{P}^*, \bar{W}^*)$ , hence both laws remain satisfied. Ratio invariance is immediate.  $\square$

Uniform gain amplification changes the level of homeostasis but not the mix: the stem-to-TD ratio remains fixed while totals rescale by  $1/A$ . In the game-theoretic view (Section 4), this corresponds to a uniform amplification of feedback sensitivity that rescales absolute abundances while preserving the Nash/ESS composition. Figure 5 visualizes the extinction-growth threshold (Theorem 5.1) and the gain-scaling symmetry (Proposition 5.6).

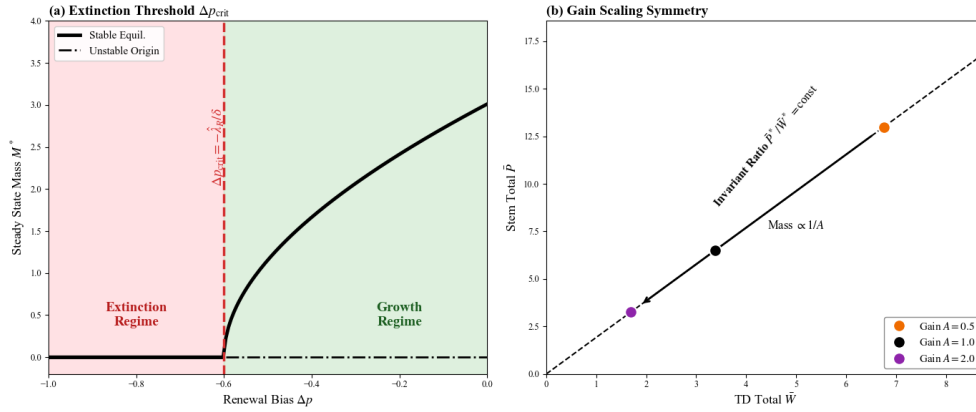


**Fig. 5** Global qualitative structure and scaling symmetry. **(a) Extinction-growth threshold** (Theorem 5.1): A stability threshold at the origin separates the extinction regime (red zone, stable origin) from the growth regime (green zone, stable interior equilibrium). The critical threshold occurs exactly at  $\Delta p_{\text{crit}}$ . **(b) Gain-scaling symmetry** (Proposition 5.6): Under uniform amplification of feedback gains ( $A \rightarrow 2A$ ), the equilibrium point shifts along a ray of constant stem-to-TD ratio (dashed line), demonstrating that tissue composition is invariant to global sensitivity scaling while total mass scales as  $1/A$ .

## 6 Numerical methods and reproducible verification

This section provides a self-contained computational counterpart to the analytical results of Sections 3–5. Following best practice for certified computational verification

**Table 1** Correspondence between analytical results and certified numerical checks.

Theorem / Result	Numerical check	Section / Figure
Theorem 3.1 (balance laws)	Certified residual bounds $R_P, R_W, R_M$	6.4, Fig. 7
Corollary 3.2 (ODE closure)	PDE totals vs. ODE	6.6, Fig. 8
Theorem 4.1 (Nash = homeostasis)	Replicator field zero-crossing	6.8, Fig. 10
Theorem 4.2 (equalization/Ratio laws)	Certified equilibrium residuals	6.11
Theorem 5.1 (threshold)	Bifurcation scan	6.9, Fig. 11
Theorem 5.4 (Dulac / no cycles)	Divergence field sign check	6.12, Fig. 13
Theorem 5.5 (global convergence)	Phase portrait convergence	6.7, Fig. 9
Proposition 5.6 (gain scaling)	Scaling invariance to $\varepsilon_{\text{mach}}$	6.10, Table 5

in mathematical biology (Oberkampf and Trucano 2002; Roache 1998), we organize the material into two layers. The first is the verification layer. Do the discrete schemes solve the stated equations accurately? The second is the certified computational check layer. Do the numerical solutions exhibit the qualitative behavior predicted by the theorems, with all reported quantities programmatically emitted by deterministic, parameter-locked scripts? Table 1 maps each main theorem to the specific verification test or certified computational check that supports it. Related recent work also stresses algebraic-spectral stability tests for explicit time-stepping schemes (e.g., forward Euler) alongside closed-form thresholds (Wang and Yu 2026), and it provides a complementary verification paradigm for mechanistic dynamical models.

## 6.1 Numerical schemes

Our PDE solver is the first-order upwind finite-volume scheme with operator splitting. We discretize the damage-structured system (5) on a uniform grid  $\{x_j = (j + \frac{1}{2})\Delta x\}_{j=0}^{N_x-1}$  over  $[0, x_{\text{max}}]$  with  $\Delta x = x_{\text{max}}/N_x$  and  $x_{\text{max}} = 10$  used for baseline runs; for closure-verification and long-horizon comparisons we increase  $x_{\text{max}}$  (Section 6.6).

Since  $v_P, v_W > 0$ , information propagates in the positive- $x$  direction and the upwind numerical flux at the interface  $x_{j+1/2}$  is

$$\mathcal{F}_{j+1/2}^P = v_P P_j^n, \quad \mathcal{F}_{j+1/2}^W = v_W W_j^n, \quad (30)$$

with  $\mathcal{F}_{1/2}^P = \mathcal{F}_{1/2}^W = 0$  enforcing the homogeneous inflow boundary condition  $P(t, 0) = W(t, 0) = 0$ . The conservative finite-volume update for the transport step is

$$P_j^{n+1, \text{tr}} = P_j^n - \frac{\Delta t}{\Delta x} (\mathcal{F}_{j+1/2}^P - \mathcal{F}_{j-1/2}^P), \quad (31)$$

and analogously for  $W_j^{n+1, \text{tr}}$ .

The birth operators  $\mathcal{B}_P, \mathcal{B}_W$  (cf. (3)) involve the dilation (push-forward) map  $[\mathcal{T}_\alpha f](x) = (1/\alpha) f(x/\alpha)$  for each inheritance fraction  $\alpha \in \{\alpha_1, \alpha_2, \gamma_1\}$  (stem branch) or  $\alpha \in \{\beta_1, \beta_2, \gamma_2\}$  (TD branch). The fundamental property driving the balance-law reduction is the mass identity  $\int_0^\infty [\mathcal{T}_\alpha f] dx = \int_0^\infty f dx$  (Lemma A.1). A discretization

that does not preserve this identity exactly would introduce a spurious mass defect that contaminates the balance-law residual (Test 3) and the PDE-vs-ODE closure check.

We therefore use a conservative finite-volume projection (flux-form remapping) rather than pointwise interpolation. Treating  $P_k$  as the cell average on  $C_k = [k\Delta x, (k+1)\Delta x]$ , the dilation maps  $C_k$  to the image interval  $\alpha C_k = [\alpha k\Delta x, \alpha(k+1)\Delta x]$  of width  $\alpha\Delta x$ . Since  $\alpha \in (0, 1)$ , this image is narrower than  $\Delta x$  and overlaps at most two target cells. We redistribute the source mass  $P_k\Delta x$  onto the target grid by exact overlap fractions:

$$[\mathcal{T}_{\alpha,h}P]_j = \frac{1}{\alpha\Delta x} \sum_{k=0}^{N_x-1} P_k \omega_{jk}(\alpha), \quad (32)$$

where  $\omega_{jk}(\alpha) := |\alpha C_k \cap C_j|$  is the length of the overlap between the image interval and target cell  $C_j$ . Because  $\sum_j \omega_{jk}(\alpha) = |\alpha C_k| = \alpha\Delta x$  for every source cell  $k$  (provided  $\alpha C_k \subset [0, x_{\max}]$ ), we obtain the exact discrete conservation identity

$$\sum_{j=0}^{N_x-1} [\mathcal{T}_{\alpha,h}P]_j \Delta x = \sum_{k=0}^{N_x-1} P_k \Delta x \quad (33)$$

to machine precision ( $\varepsilon_{\text{mach}} \approx 2.2 \times 10^{-16}$ ). The overlap weights  $\omega_{jk}$  are nonzero only for  $j \in \{j_L(k), j_L(k) + 1\}$  with  $j_L(k) = \lfloor \alpha k \rfloor$ , so the operation is  $\mathcal{O}(N_x)$  and implemented via vectorized scatter-add.

The full discrete birth operators are then assembled as in the continuous case:

$$[\mathcal{B}_{P,h}]_j = p_1(\bar{W}_h) \lambda_P(\bar{W}_h) ([\mathcal{T}_{\alpha_1,h}P]_j + [\mathcal{T}_{\alpha_2,h}P]_j) + p_3(\bar{W}_h) \lambda_P(\bar{W}_h) [\mathcal{T}_{\gamma_1,h}P]_j,$$

and analogously for  $\mathcal{B}_{W,h}$ . By linearity of (33) and  $p_1 + p_2 + p_3 = 1$ , this yields the exact discrete analogue of Lemma A.2:

$$\sum_j [\mathcal{B}_{P,h} + \mathcal{B}_{W,h}]_j \Delta x = 2 \lambda_P(\bar{W}_h) \bar{P}_h.$$

We use first-order operator splitting: given  $(P^n, W^n)$  at  $t^n$ , we first advance the transport step by (31) (and its analogue for  $W$ ), obtaining  $(P^{n+1,\text{tr}}, W^{n+1,\text{tr}})$ . We then update the reaction step by forward Euler,

$$P_j^{n+1} = P_j^{n+1,\text{tr}} + \Delta t \left( [\mathcal{B}_{P,h}[P^{n+1,\text{tr}}]]_j - \lambda_P(\bar{W}_h^{n+1,\text{tr}}) P_j^{n+1,\text{tr}} + \lambda_R(\bar{P}_h^{n+1,\text{tr}}) W_j^{n+1,\text{tr}} \right), \quad (34)$$

$$W_j^{n+1} = W_j^{n+1,\text{tr}} + \Delta t \left( [\mathcal{B}_{W,h}[P^{n+1,\text{tr}}]]_j - (\delta + \lambda_R(\bar{P}_h^{n+1,\text{tr}})) W_j^{n+1,\text{tr}} \right),$$

where  $\bar{P}_h^{n+1,\text{tr}} = \sum_j P_j^{n+1,\text{tr}} \Delta x$  and  $\bar{W}_h^{n+1,\text{tr}} = \sum_j W_j^{n+1,\text{tr}} \Delta x$ . Time integration is performed under the CFL restriction

$$\Delta t \leq \text{CFL} \cdot \frac{\Delta x}{\max(v_P, v_W)}, \quad \text{CFL} = 0.8. \quad (35)$$

To suppress rare floating-point undershoots, we apply a positivity fix only when  $\min_j P_j^{n+1} < -10^{-14}$  or  $\min_j W_j^{n+1} < -10^{-14}$ , by setting negative values to zero. We record the induced mass defect at each step and verify it remains below  $10^{-12}$  relative to total mass in all runs reported here.

Because the scheme is first-order in both the transport upwinding and the operator splitting, we expect  $\mathcal{O}(\Delta x)$  convergence of the integrated quantities  $\bar{P}(t), \bar{W}(t)$ ; this is confirmed in Section 6.2.

We now turn to the ODE solver. The exact two-compartment closure (11) is integrated using an adaptive Runge–Kutta method with error control. The exact two-compartment closure (11) is integrated using the Dormand–Prince RK4(5) pair (RK45), with relative tolerance  $\varepsilon_{\text{rel}} = 10^{-10}$  and absolute tolerance  $\varepsilon_{\text{abs}} = 10^{-12}$ . These stringent tolerances ensure that the ODE solution serves as a reference truth against which PDE totals can be compared. For verification, we also cross-check against the eighth-order Dormand–Prince method (DOP853) and the implicit Radau IIA(5) solver; agreement to  $\mathcal{O}(10^{-10})$  confirms that temporal truncation error is negligible (Section 6.3).

Interior equilibria of (11) are characterised by the one-dimensional root condition  $r(\bar{W}) = 0$  (cf. (26)), where

$$r(\bar{W}) := \delta (p_2(\bar{W}) - p_1(\bar{W})) - \lambda_R \left( \frac{\delta \bar{W}}{\lambda_P(\bar{W})} \right). \quad (36)$$

The companion coordinate is recovered from the Ratio law:  $\bar{P}^* = \delta \bar{W}^* / \lambda_P(\bar{W}^*)$ .

For the reference parameter set (Table 2), Algorithm 1 detects exactly one sign change of  $r(\bar{W})$  and returns a unique interior equilibrium  $(\bar{P}^*, \bar{W}^*)$ . The Equalization law, Ratio law, and ODE steady-state residuals are all satisfied to double-precision accuracy (see Section 6.11).

---

**Algorithm 1** Bracket-and-refine Nash solver

---

**Require:** Feedback maps  $p_1, p_2, \lambda_P, \lambda_R$ ; death rate  $\delta > 0$ ; search interval  $[\bar{W}_{\min}, \bar{W}_{\max}]$ ; tolerance  $\varepsilon$ .

**Ensure:** List of certified interior equilibria  $\{(\bar{P}_k^*, \bar{W}_k^*)\}$ .

- 1: Evaluate  $r(\bar{W})$  on a log-spaced grid of  $N_{\text{grid}} = 2000$  points in  $[\bar{W}_{\min}, \bar{W}_{\max}]$ .
  - 2: **for all** consecutive pairs  $(r_j, r_{j+1})$  with  $r_j r_{j+1} < 0$  **do**
  - 3:     Apply Brent’s method on  $[\bar{W}_j, \bar{W}_{j+1}]$  with tolerance  $\varepsilon$  to obtain  $\bar{W}^*$ .
  - 4:     Set  $\bar{P}^* = \delta \bar{W}^* / \lambda_P(\bar{W}^*)$ .
  - 5:     Certify: evaluate both equilibrium laws (16)–(17) and the ODE right-hand side at  $(\bar{P}^*, \bar{W}^*)$ ; accept if all residuals are  $< 10\varepsilon$ .
  - 6: **end for**
- 

All verification tests use the reference parameter set recorded in Table 2. Initial data for the PDE are Gaussian bumps (rapidly decaying to working precision):  $P_0(x) = \exp(-(x-2)^2/0.5)$  and  $W_0(x) = 0.5 \exp(-(x-1.5)^2/0.5)$ .

**Table 2** Reference parameter set for all numerical experiments. The compensatory feedback conditions of Definition 5.3 are satisfied:  $\Delta(\bar{W}) := p_2(\bar{W}) - p_1(\bar{W}) > 0$  and  $\Delta'(\bar{W}) < 0$  for all  $\bar{W} \geq 0$  (verified numerically for the Hill families with these parameters).

Symbol	Description	Value
$\hat{p}_1$	Baseline self-renewal probability	0.20
$\hat{p}_2$	Baseline symmetric differentiation	0.40
$\hat{\lambda}_P$	Baseline stem division rate	1.0
$\hat{\lambda}_R$	Baseline dedifferentiation rate	0.3
$k_1, k_2, k_3, k_4$	Hill gains	0.5
$m_1, m_2, m_3, m_4$	Hill exponents	2
$\delta$	Uniform TD death rate	0.5
$v_P, v_W$	Transport (damage accumulation) speeds	1.0
$\alpha_i, \beta_i, \gamma_i$	Symmetric damage inheritance	0.5

## 6.2 Test 1: PDE grid convergence

We run the PDE solver on four successively refined grids  $N_x \in \{100, 200, 400, 800\}$  with  $T = 5$  and compare the computed total masses  $\bar{P}(t), \bar{W}(t)$  against the finest grid. Table 3 reports the  $L^\infty$ -norm of the inter-grid differences and the estimated convergence rates. Figure 6 shows the consistency of the stem and TD mass across different spatial resolutions.

**Table 3** Grid convergence of PDE totals ( $T = 5$ , CFL = 0.8). Differences are measured in  $L^\infty([0, T])$  between consecutive refinements.

$N_x^{\text{coarse}}$	$N_x^{\text{fine}}$	$\ \Delta P\ _\infty$	$\ \Delta W\ _\infty$	rate ( $P$ )	rate ( $W$ )
100	200	$1.80 \times 10^{-3}$	$6.19 \times 10^{-3}$	—	—
200	400	$8.69 \times 10^{-4}$	$2.97 \times 10^{-3}$	1.05	1.06
400	800	$4.27 \times 10^{-4}$	$1.46 \times 10^{-3}$	1.02	1.03

The rates are consistent with the expected first-order convergence of the upwind scheme in the integrated  $L^1$  sense. Higher-order accuracy could be attained with slope-limited MUSCL reconstruction, but is not pursued here since the primary analytical conclusions rest on the exact ODE closure.

## 6.3 Test 2: ODE time-step and method independence

We integrate the exact closure (11) with  $\Delta t_{\text{max}} \in \{0.1, 0.05, 0.025, 0.0125\}$  and compare to the finest-step trajectory at  $T = 10$ . Trajectory differences are  $\mathcal{O}(10^{-11} - 10^{-12})$  throughout, confirming that temporal truncation error is negligible relative to other error sources. Cross-method comparison (RK45 vs. DOP853 vs. Radau IIA) yields agreement to  $\mathcal{O}(10^{-10} - 10^{-11})$ , providing independent confirmation.

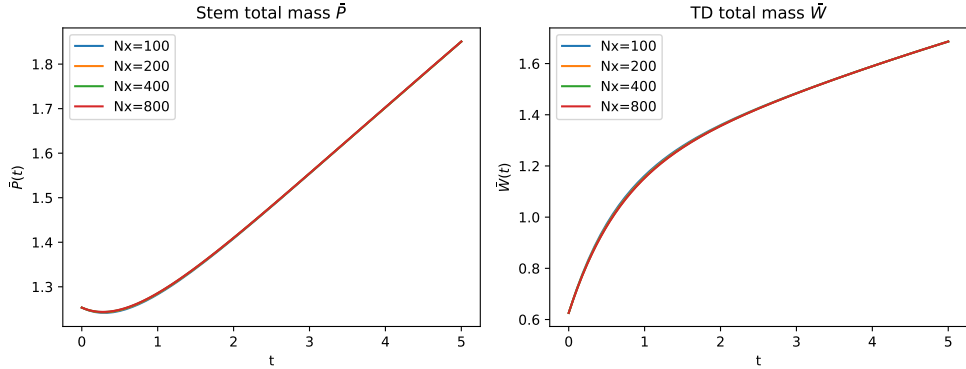


**Fig. 6 Stem and TD total mass consistency under grid refinement tests. (a) Stem mass consistency:** Time evolution of the total stem population  $\bar{P}(t)$  simulated on uniform grids with  $N_x \in \{100, 200, 400, 800\}$ . The trajectories for different resolutions overlap, indicating solution stability. **(b) TD mass consistency:** Corresponding dynamics for the TD population  $\bar{W}(t)$ , exhibiting similar robustness to spatial discretization.

### 6.4 Test 3a: Balance-law residual

Under uniform death  $\delta(x) \equiv \delta$ , Theorem 3.1 and Corollary 3.2 predict exact closure of the total-mass dynamics. To ensure we are verifying the closure rather than measuring domain-truncation artefacts (cf. Section 6.6), we use  $x_{\max} = 20$  with  $N_x = 1600$  ( $\Delta x \approx 0.0125$ ).

We define the computed balance residuals for the stem compartment as

$$R_P(t) := \left. \frac{d\bar{P}_h}{dt} \right|_{\text{num}} - \left[ (p_1(\bar{W}_h) - p_2(\bar{W}_h)) \lambda_P(\bar{W}_h) \bar{P}_h + \lambda_R(\bar{P}_h) \bar{W}_h \right], \quad (37)$$

i.e. the numerical time derivative minus the exact right-hand side of the  $\bar{P}$ -balance law (10). The analogous residual  $R_W(t)$  is defined using the  $\bar{W}$ -equation. As an independent cross-check, we compute the total-mass residual  $R_M(t)$  both as  $R_P(t) + R_W(t)$  and directly from the total-mass identity  $\dot{M} = \lambda_P(\bar{W})\bar{P} - \delta\bar{W}$ ; agreement between these two forms (to machine epsilon,  $\approx 4 \times 10^{-16}$ ) provides an additional verification point.

At  $T = 5$ , we observe  $\|R_P\|_\infty, \|R_W\|_\infty, \|R_M\|_\infty$  at the  $\mathcal{O}(10^{-3})$  level (Figure 7). A domain-sensitivity check confirms that these residuals are independent of  $x_{\max}$  (identical at  $x_{\max} \in \{10, 15, 20\}$  for  $T = 5$ ): at this time horizon the density support has not reached  $x_{\max} = 10$ , so truncation does not contaminate the residual. The magnitudes of residuals decrease under grid refinement, confirming that the balance laws hold to the accuracy of the spatial discretization.

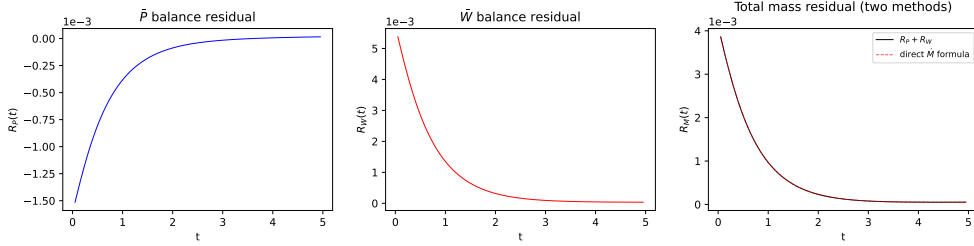


**Fig. 7 Temporal evolution of the stem, TD, and total mass residuals.** The computed residuals for stem (a) and TD (b) masses remain bounded at the  $\mathcal{O}(10^{-3})$  level, reflecting the expected first-order accuracy of the upwind finite-volume discretization. (c) **Total mass residual consistency:** Consistency of  $R_M(t)$  obtained from both the  $R_P(t) + R_W(t)$  and the total-mass identity  $\dot{M} = \lambda_P(\bar{W})\bar{P} - \delta\bar{W}$ .

### 6.5 Test 3b: Identifiability check for uniform death via effective mortality

When  $\delta(x)$  is non-constant, the mortality flux in (10) cannot be written as  $\delta\bar{W}(t)$  and the two-dimensional closure (11) fails in general (Section 3.3, Fig. 3). A diagnostic quantity that makes this failure explicit is the *effective mortality*

$$\delta_{\text{eff}}(t) := \frac{\int_0^\infty \delta(x)W(t,x) dx}{\bar{W}(t)} \quad (\bar{W}(t) > 0). \quad (38)$$

Exact closure on totals would require  $\delta_{\text{eff}}(t) \equiv \delta$  to be constant in time. Hence, any time-variation of  $\delta_{\text{eff}}(t)$  provides a direct, quantitative certificate that the uniform-death reduction is not valid for the simulated (or measured) regime. In our uniform-death reference setting, (38) is constant to machine precision; under damage-dependent  $\delta(x)$  (not shown),  $\delta_{\text{eff}}(t)$  varies in time and the closure residuals increase accordingly, consistent with the mechanism in Fig. 3.

If  $\delta(x)$  is weakly state-dependent, then  $\delta_{\text{eff}}(t)$  may remain approximately constant, yielding an approximate low-dimensional closure. Quantifying this approximation (e.g., via moment augmentation) is a natural extension, but is not required for the exact reduction results presented here.

We now present numerical solutions that independently corroborate each main theorem, providing a figure-by-figure correspondence between analytical predictions and computed behaviour.

### 6.6 PDE totals vs. exact ODE closure (Corollary 3.2)

As a direct check that the PDE total masses satisfy the closed ODE, we integrate both the full PDE and the two-dimensional ODE from matched initial conditions over  $T = 15$ .

Because the PDE is posed on a truncated domain  $[0, x_{\text{max}}]$  with zero padding beyond  $x_{\text{max}}$  in the birth-operator interpolation, mass whose damage coordinate

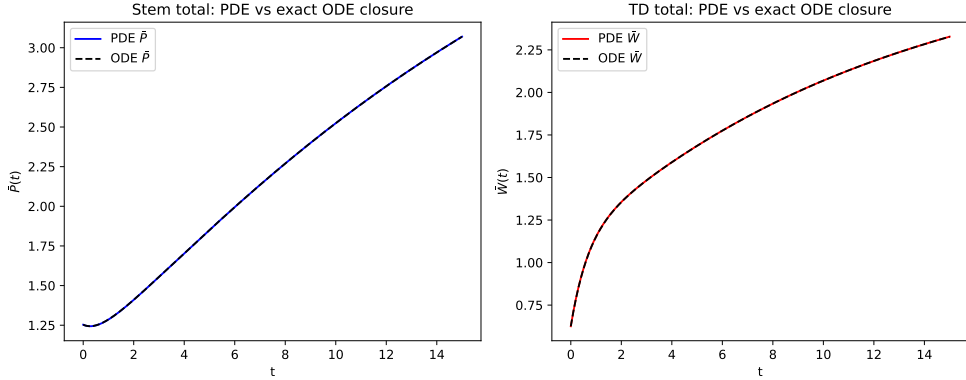


**Fig. 8 Temporal evolution of the stem and TD total masses. (a) Stem total consistency:** The consistency of stem totals obtained from integrating the PDE solution and from solving the stem-total ODE. The overlap between the solid line (PDE) and the dashed line (ODE) validates the exact ODE closure. **(b) TD total consistency:** The consistency of TD totals obtained from the same way as the stem totals.

exceeds  $x_{\max}$  is negligible. To isolate this artefact from the spatial discretization error, we fix  $\Delta x \approx 0.0125$  and vary  $x_{\max} \in \{10, 15, 20\}$  (scaling  $N_x$  proportionally). The PDE-vs-ODE discrepancy drops from  $\mathcal{O}(10^{-1})$  at  $x_{\max} = 10$  to  $\mathcal{O}(10^{-3})$  at  $x_{\max} = 15$  and  $\mathcal{O}(10^{-4})$  at  $x_{\max} = 20$ , confirming that the dominant error source at  $x_{\max} = 10$  is domain truncation rather than spatial discretization.

With  $x_{\max} = 20$  (sufficiently large that truncation effects are negligible), the PDE-vs-ODE discrepancy in  $\|\bar{P}_{\text{PDE}} - \bar{P}_{\text{ODE}}\|_{L^\infty[0,T]}$  decreases under grid refinement at the expected first-order rate (Table 4), directly corroborating that the closure is exact and the remaining error is entirely due to the  $\mathcal{O}(\Delta x)$  upwind scheme. Figure 8 shows the tight consistency between the totals in the PDE and the ODE models. The positivity-fix mass defect is zero in all runs.

**Table 4** PDE-vs-ODE closure error under grid refinement ( $x_{\max} = 20$ ,  $T = 15$ ). All entries are programmatically emitted.

$N_x$	$\Delta x$	$\ \Delta P\ _\infty$	$\ \Delta W\ _\infty$	rate ( $P$ )
400	0.050	$1.72 \times 10^{-3}$	$5.86 \times 10^{-3}$	—
800	0.025	$8.50 \times 10^{-4}$	$2.89 \times 10^{-3}$	1.02
1600	0.0125	$4.23 \times 10^{-4}$	$1.44 \times 10^{-3}$	1.01
3200	0.00625	$2.11 \times 10^{-4}$	$7.16 \times 10^{-4}$	1.00

## 6.7 Phase portrait with nullclines (Theorems 5.1 and 5.5)

Figure 9 shows the  $(\bar{P}, \bar{W})$  phase plane with: (i) the  $\dot{\bar{P}} = 0$  nullcline and the  $\dot{\bar{W}} = 0$  nullcline, computed by solving the respective implicit equations via bisection; (ii) a normalized vector field (arrows colored by speed); (iii) eight trajectories launched from diverse initial conditions in  $(0, \infty)^2$ , integrated with RK45 to  $T = 30$ . All trajectories converge monotonically to the unique interior equilibrium  $(\bar{P}^*, \bar{W}^*)$ , with no oscillations or spiraling, consistent with the strictly negative divergence established in Theorem 5.4 and the global convergence result of Theorem 5.5. The origin  $(0, 0)$  is a saddle, confirming the growth regime: for the reference parameters,  $\Delta p = \hat{p}_1 - \hat{p}_2 = -0.20$  while  $\Delta p_{\text{crit}} = -\hat{\lambda}_R/\delta = -0.60$ , so  $\Delta p > \Delta p_{\text{crit}}$  (Theorem 5.1).

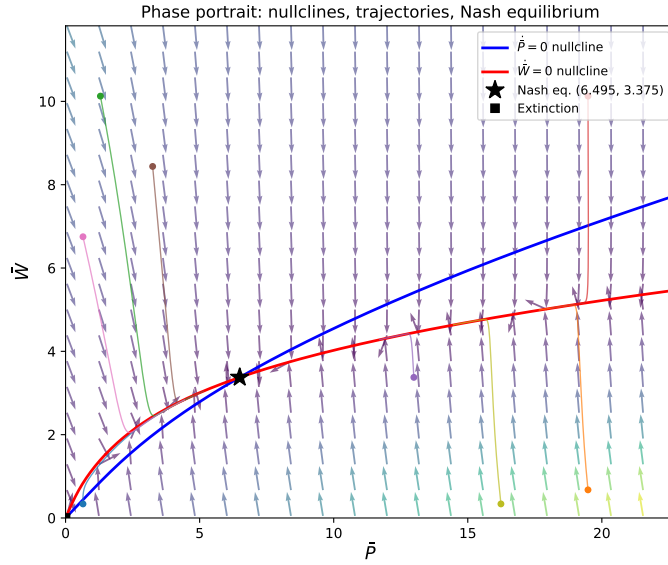


**Fig. 9** Phase portrait of (18). The isoclines where the net growth rates vanish ( $\dot{\bar{P}} = 0$ , blue) and ( $\dot{\bar{W}} = 0$ , orange) divide the phase space into regions of monotonic increase or decrease. Their intersection defines the unique positive equilibrium  $(\bar{P}^*, \bar{W}^*)$ , representing the homeostatic tissue size. Sample trajectories (gray curves) initiated from various total mass configurations all converge to the equilibrium, numerically confirming the global stability guaranteed by the Bendixson–Dulac criterion.

## 6.8 Replicator field and Nash frequency (Theorem 4.1)

Figure 10 plots  $\dot{s} = s(1-s)(F_P - F_W)$  as a function of the stem frequency  $s = \bar{P}/M$  for several fixed values of the total mass  $M \in \{0.3M^*, 0.6M^*, M^*, 1.5M^*, 2.5M^*\}$ , where  $M^* = \bar{P}^* + \bar{W}^*$ . In every case the replicator field has a unique zero-crossing at the Nash/homeostasis frequency  $s^*$  predicted by Theorem 4.1 and the equilibrium laws (16)–(17). For  $s < s^*$  the field is positive ( $\dot{s} > 0$ : stem fraction increasing), and

for  $s > s^*$  it is negative ( $\dot{s} < 0$ : stem fraction decreasing), confirming that  $s^*$  is a stable rest point of the replicator equation (15) and hence an ESS of the induced two-phenotype game.

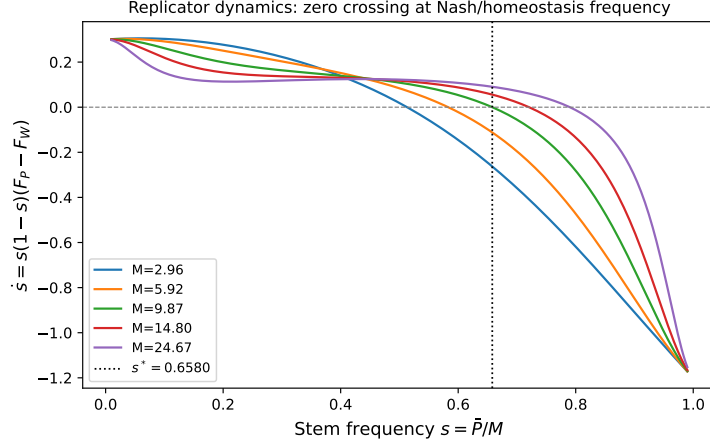


**Fig. 10 Stem frequency**  $\dot{s} = s(1-s)(F_P - F_W)$ . The rate of change of stem frequency  $\dot{s}$  is plotted against  $s$  for fixed total mass values  $M \in \{0.3M^*, 0.6M^*, M^*, 1.5M^*, 2.5M^*\}$ . The dynamics are governed by the replicator equation  $\dot{s} = s(1-s)(F_P - F_W)$ . All curves intersect  $\dot{s} = 0$  at a unique interior frequency  $s^*$ , corresponding to the unique Nash equilibrium where the per-capita payoffs equalize ( $F_P = F_W$ ). The negative slope at  $s^*$  indicates that the equilibrium is evolutionarily stable (ESS), driving the population composition toward the homeostatic ratio regardless of the initial fraction.

## 6.9 Bifurcation scan in $\Delta p$ and $\delta$ (Theorem 5.1)

Figure 11 presents one-parameter continuation scans of the interior equilibrium as  $\Delta p := \hat{p}_1 - \hat{p}_2$  and  $\delta$  are varied independently, with all other parameters held at their reference values (Table 2). In panel (a),  $\Delta p$  is implemented through the admissible affine parameterization  $\hat{p}_1 = (0.8 + \Delta p)/3$  and  $\hat{p}_2 = (0.8 - 2\Delta p)/3$ , so that  $\hat{p}_1 - \hat{p}_2 = \Delta p$  while the critical value  $\Delta p_{\text{crit}} = -\hat{\lambda}_R/\delta$  remains in the interior of the scan window.

Theorem 5.1 establishes  $\Delta p_{\text{crit}} = -\hat{\lambda}_R/\delta$  as a local threshold at the origin: for  $\Delta p < \Delta p_{\text{crit}}$  the origin is locally asymptotically stable, while for  $\Delta p > \Delta p_{\text{crit}}$  it is a saddle with an unstable manifold. In the present parameter family that satisfies the hypotheses of Theorems 5.2–5.5 throughout the scan range, the local instability of the origin coincides with the appearance of a unique positive equilibrium. Numerically, panel (a) resolves this branch over the admissible window  $\Delta p \in [-0.8, 0.4]$  determined by the chosen affine parameterization of  $(\hat{p}_1, \hat{p}_2)$ . The branch is omitted, rather than plotted at zero, whenever the probability constraints fail or the one-dimensional root solver detects no interior equilibrium. Within the displayed admissible range, the threshold  $\Delta p_{\text{crit}} = -0.6$  lies in the interior of the scan and separates the extinction regime from the positive branch. Near  $\Delta p = 0^-$  the equilibrium masses grow rapidly,

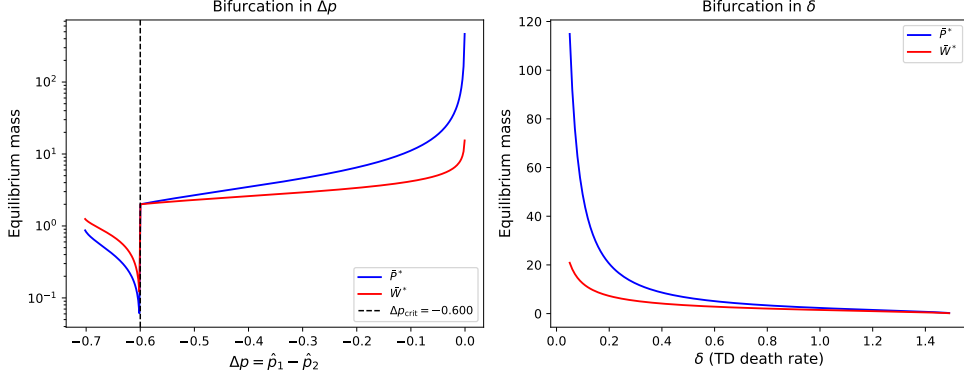


**Fig. 11 One-parameter continuation scans.** (a) **Critical threshold:** The equilibrium stem mass  $\bar{P}^*$  (blue) and TD mass  $\bar{W}^*$  (orange) are plotted against the renewal bias  $\Delta p = \hat{p}_1 - \hat{p}_2$  using the affine parameterization  $\hat{p}_1 = (0.8 + \Delta p)/3$ ,  $\hat{p}_2 = (0.8 - 2\Delta p)/3$ . Both curves are displayed on a semilogarithmic scale. Gaps indicate parameter values for which either the probabilities are inadmissible or no positive equilibrium is detected. The dashed line marks  $\Delta p_{\text{crit}} = -\hat{\lambda}_R/\delta$ . (b) **Mortality sensitivity:** Dependence of the equilibrium masses on the TD death rate  $\delta$ . As mortality increases, the homeostatic tissue size contracts until extinction.

so the semilogarithmic presentation is used to display the large variation in scale without conflating nonexistence with vanishing mass. In the  $\delta$ -scan, increasing  $\delta$  shifts the equilibrium toward smaller total mass, primarily by increasing the net loss term in the  $\bar{W}$ -equation. No secondary bifurcation or multi-stability is observed in this parameter family.

## 6.10 Gain-scaling invariance (Proposition 5.6)

Proposition 5.6 predicts that under uniform amplification  $k_i \mapsto Ak_i$  ( $i = 1, \dots, 4$ ), the equilibrium rescales as  $(\bar{P}^*, \bar{W}^*) \mapsto (\bar{P}^*/A, \bar{W}^*/A)$  while the ratio  $\bar{P}^*/\bar{W}^*$  is invariant. Table 5 confirms this to machine precision (ratio errors  $\leq 3 \times 10^{-15}$  for all  $A$  tested), providing a stringent check that both the analytical scaling law and the numerical root-finder are correct. Figure 12 shows the scaling of equilibrium levels and invariance of ratios under uniform scaling.

**Table 5** Gain-scaling test: equilibrium under  $k_i \mapsto Ak_i$ . Let  $\bar{P}_{A=1}^*, \bar{W}_{A=1}^*$  denote the equilibrium at  $A = 1$ . The ratio  $\bar{P}^*/\bar{W}^*$  is invariant to machine precision.

$A$	$P^*$	$W^*$	$P_A^*/(P_{A=1}^*/A)$	$P^*/W^*$	ratio error
0.5	12.9890	6.7507	1.0000	1.9241	$2.89 \times 10^{-15}$
1.0	6.4945	3.3753	1.0000	1.9241	$0.00 \times 10^0$
2.0	3.2473	1.6877	1.0000	1.9241	$2.89 \times 10^{-15}$
4.0	1.6236	0.8438	1.0000	1.9241	$2.89 \times 10^{-15}$
8.0	0.8118	0.4219	1.0000	1.9241	$2.89 \times 10^{-15}$

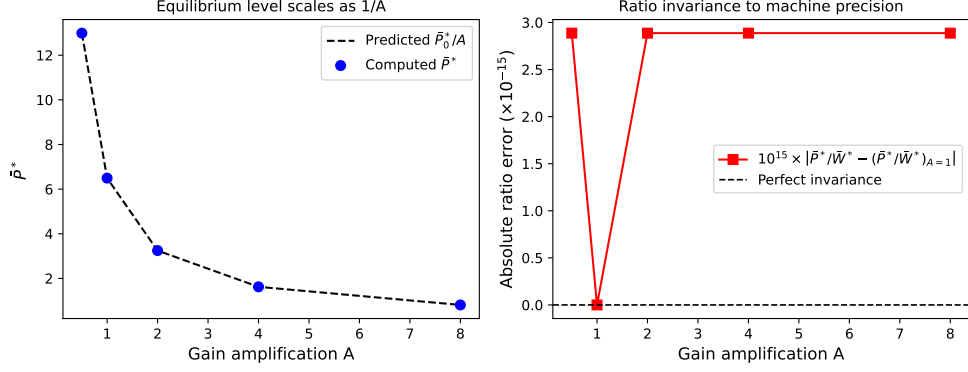


**Fig. 12 Rescaling of the equilibrium and invariance of population ratio.** (a) **Gain rescaling:** The equilibrium stem mass  $\bar{P}^*$  (blue dot) and predicted stem mass from Proposition 5.6  $\bar{W}^*$  (dashed curve) are plotted as a function of the feedback gain scaling factor  $A$ . As predicted by Proposition 5.6, increasing the sensitivity of the feedback loops ( $A \rightarrow 8.0$ ) scales the total tissue mass down exactly by  $1/A$ . (b) **Ratio invariance:** Rather than plotting the nearly constant raw ratio  $\bar{P}^*/\bar{W}^*$ , the panel reports the absolute deviation from the  $A = 1$  baseline ratio in units of  $10^{-15}$ . The deviations remain at machine precision across all tested scalings, confirming that the composition is invariant up to roundoff error.

### 6.11 Certified Nash equilibrium computation (Theorem 4.2)

Algorithm 1 returns a unique interior equilibrium  $(\bar{P}^*, \bar{W}^*)$ . The certification step evaluates four independent residual bounds:

Certified residual	Bound
Equalization law: $ (p_2(\bar{W}^*) - p_1(\bar{W}^*))\delta - \lambda_R(\bar{P}^*) $	$< 10^{-16}$
Ratio law: $ \bar{P}^*/\bar{W}^* - \delta/\lambda_P(\bar{W}^*) $	$= 0$
ODE RHS: $ \dot{\bar{P}} $ at $(\bar{P}^*, \bar{W}^*)$	$< 10^{-15}$
ODE RHS: $ \dot{\bar{W}} $ at $(\bar{P}^*, \bar{W}^*)$	$< 10^{-15}$

All residuals are at or below double-precision machine epsilon ( $\approx 2.2 \times 10^{-16}$ ), certifying the equilibrium to the maximum attainable numerical accuracy.

### 6.12 Negative divergence field (Theorem 5.4)

Figure 13 displays the divergence  $\nabla \cdot \mathbf{G}(\bar{P}, \bar{W})$  of the reduced vector field, computed by centered finite differences on a  $200 \times 200$  grid over  $[0.01, 3.5\bar{P}^*] \times [0.01, 3.5\bar{W}^*]$ . The divergence is strictly negative at every sampled grid point; the supremum over all  $200 \times 200$  evaluation points satisfies  $\sup \nabla \cdot \mathbf{G} < 0$ . No zero-level contour appears. This is consistent with the analytical result of Theorem 5.4, which establishes strict negativity on all of  $(0, \infty)^2$ ; the numerical check provides independent corroboration on the sampled subdomain.

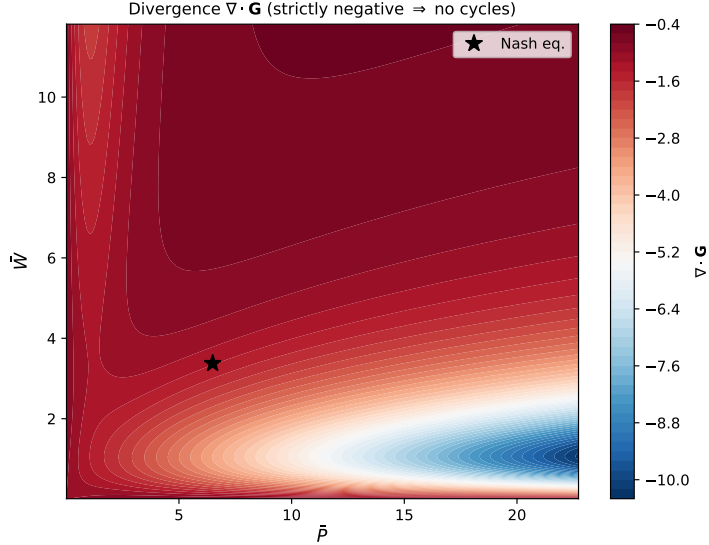


**Fig. 13 Heatmap of the divergence  $\nabla \cdot G$ .** Heatmap of the vector field divergence  $\nabla \cdot G = \partial_{\bar{P}} \dot{\bar{P}} + \partial_{\tilde{W}} \dot{\tilde{W}}$  across the phase space. The divergence is strictly negative everywhere, satisfying the Bendixson–Dulac criterion (with weighting function  $\varphi \equiv 1$ ) and rigorously precluding the existence of periodic orbits. This global contraction of phase volume guarantees that all trajectories in the positive quadrant must converge to the unique homeostatic equilibrium.

## 7 Case study: murine intestinal crypt homeostasis and regeneration

We illustrate the modeling pipeline on the murine small-intestinal crypt, a canonical fast-renewing tissue in which stem-cell numbers, turnover times, and injury-induced plasticity are unusually well quantified. In this system,  $Lgr5^+$  crypt-base-columnar (CBC) stem cells sustain epithelial renewal under homeostasis and can be replenished after injury through progenitor-cell plasticity and dedifferentiation, making the crypt a natural biological testbed for the equilibrium laws and regeneration dynamics derived in Sections 4–5 (Snippert et al. 2010; Hagemann et al. 1970; Van Der Flier and Clevers 2009; Murata et al. 2020).

### 7.1 Biological context and aggregate calibration targets

Quantitative lineage-tracing experiments indicate that a murine small-intestinal crypt contains approximately  $14 \pm 2$   $Lgr5^{\text{hi}}$  stem cells, and that these cells divide roughly once per day under homeostatic conditions (Snippert et al. 2010). At the tissue level, the intestinal epithelium renews on a  $\sim 4$ –5 day timescale (Van Der Flier and Clevers 2009). As an aggregate calibration target for the present two-compartment reduction, we take the total crypt cellularity to be approximately 292 cells, so that after assigning 14 cells to the  $Lgr5^+$  stem compartment, the remaining  $\sim 278$  cells define the effective TD compartment used below (Hagemann et al. 1970).

To probe regeneration, we use the radiation-injury paradigm. Lgr5-marked CBC cells are highly radiosensitive and are strongly depleted after irradiation, while subsequent crypt recovery requires restoration of the stem-cell pool (Richmond et al. 2016). Recent lineage-tracing work further shows that this restoration is driven in large part by ASCL2-dependent dedifferentiation of committed absorptive and secretory progenitors back into the stem state (Murata et al. 2020). These observations provide a natural dynamical perturbation against which to compare the reduced model.

## 7.2 Mapping the crypt onto the two-compartment reduction

We identify the model stem compartment  $P$  with the Lgr5<sup>+</sup> CBC population and the effective TD compartment  $W$  with all remaining crypt-resident TD cells. This lumped  $W$ -compartment includes both transit-amplifying progenitors and more mature epithelial lineages. Accordingly, the present case study should be read as an aggregate coarse-graining of the crypt rather than as a one-to-one transcriptional cell-state model.

We set the effective loss rate in the  $W$ -compartment to

$$\delta = \frac{1}{4} \text{ day}^{-1},$$

corresponding to a representative 4-day epithelial turnover time. The homeostatic aggregate calibration targets are therefore

$$(\bar{P}^*, \bar{W}^*) = (14, 278), \quad s^* = \frac{\bar{P}^*}{\bar{P}^* + \bar{W}^*} = \frac{14}{292} = 0.0479.$$

## 7.3 Calibration from the equilibrium laws

A central advantage of the theory is that the homeostatic equilibrium is constrained algebraically by the Ratio law and Equalization law of Theorem 4.2. Substituting the crypt targets  $(\bar{P}^*, \bar{W}^*) = (14, 278)$  and  $\delta = 1/4$  into the Ratio law gives

$$\lambda_P(\bar{W}^*) = \delta \frac{\bar{W}^*}{\bar{P}^*} = \frac{1}{4} \frac{278}{14} \approx 4.9643 \text{ day}^{-1}.$$

This value should be interpreted as an *aggregate effective production rate* in the two-compartment coarse-graining, not as the literal single-cell cycling rate of an Lgr5<sup>+</sup> CBC cell. Biologically, this distinction is expected: the present reduction lumps the transit-amplifying cascade into the effective TD compartment, so the net stem-to-output flux is amplified relative to the  $\sim 1$  division/day CBC rate (Snippert et al. 2010).

We then calibrate Hill-type feedback maps to place the interior equilibrium exactly at the chosen aggregate target. The calibrated parameter set returned by the script is

$$\begin{aligned} \hat{p}_1 &= 0.076603, & \hat{p}_2 &= 0.222652, \\ k_{p_1} &= 0.004260, & k_{p_2} &= 0.004260, \end{aligned}$$

$$\begin{aligned}\hat{\lambda}_P &= 5.884502 \text{ day}^{-1}, & k_{\lambda_P} &= 0.001549, \\ \hat{\lambda}_R &= 0.039233 \text{ day}^{-1}, & k_{\lambda_R} &= 0.089821,\end{aligned}$$

with Hill exponents fixed at

$$m_{p_1} = m_{p_2} = m_{\lambda_P} = m_{\lambda_R} = 2, \quad \delta = 0.25 \text{ day}^{-1}.$$

For this calibrated model, the optimization objective is  $7.158 \times 10^{-28}$ , the selected equilibrium is

$$(\bar{P}^*, \bar{W}^*) = (14.0000, 278.0000),$$

the equalization residual is  $-1.735 \times 10^{-18}$ , and the ratio residual is  $6.939 \times 10^{-18}$ . Thus, the equilibrium laws are satisfied up to numerical roundoff, and the reduced system reproduces the prescribed aggregate homeostatic state exactly at floating-point precision.

## 7.4 Homeostasis as payoff equalization

Under this calibration, the crypt homeostatic state is simultaneously: (i) the interior equilibrium of the reduced two-compartment system, (ii) the intersection of the ratio and Equalization laws, and (iii) the interior rest point of the induced replicator equation for the stem frequency

$$s(t) = \frac{\bar{P}(t)}{\bar{P}(t) + \bar{W}(t)}.$$

Its equilibrium composition is

$$s^* = 0.0479,$$

that is, a stem fraction of approximately 4.79%.

In the game-theoretic interpretation of Section 4, this means that intestinal crypt homeostasis corresponds to payoff equalization between the stem and TD phenotypes:

$$F_P(\bar{P}^*, \bar{W}^*) = F_W(\bar{P}^*, \bar{W}^*) = 0.$$

Thus, the stem phenotype is not maintained because it is intrinsically dominant, but because feedback-regulated lineage dynamics drive the system to a composition at which neither phenotype has a per-capita growth advantage. In this sense, crypt homeostasis is an induced Nash equilibrium of the reduced population game. Figure 14 shows murine intestinal crypt homeostasis and regeneration in the calibrated two-compartment reduction.

## 7.5 Post-injury regeneration and the role of dedifferentiation

To connect the equilibrium theory with regeneration, we consider an irradiation-like perturbation in which the  $\text{Lgr5}^+$  compartment is sharply depleted from its homeostatic level, mimicking the experimentally observed radiosensitivity of CBC stem cells (Richmond et al. 2016). In the numerical case study, the subsequent recovery trajectory is

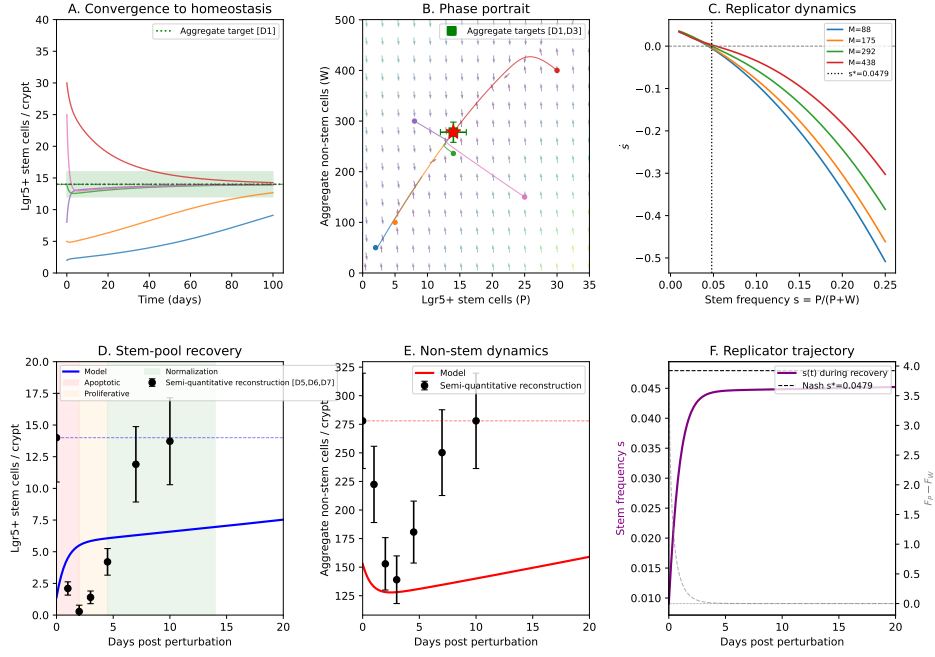


**Fig. 14 Murine intestinal crypt homeostasis and regeneration in the calibrated two-compartment reduction. (A) Convergence to the homeostatic aggregate state.** Trajectories from diverse initial conditions converge to the calibrated equilibrium  $(\bar{P}^*, \bar{W}^*) = (14, 278)$ , corresponding to a stem fraction  $s^* = \bar{P}^*/(\bar{P}^* + \bar{W}^*) = 0.0479$ . **(B) Phase portrait and literature-based homeostatic target.** The nullclines of the reduced system intersect at the unique positive equilibrium. The highlighted target point corresponds to the aggregate homeostatic crypt state used for calibration, with approximately 14 Lgr5<sup>+</sup> stem cells and  $\sim 292$  total crypt cells. **(C) Replicator dynamics and payoff equalization.** The induced frequency dynamics  $\dot{s} = s(1-s)(F_P - F_W)$  admit a unique interior rest point at  $s^* = 0.0479$ , showing that homeostasis corresponds to payoff equalization between stem and TD phenotypes. **(D) Stem-pool recovery after irradiation-like depletion.** Following acute depletion of the stem compartment, the model trajectory returns toward the homeostatic state. Black points denote a semi-quantitative reconstruction of the published post-irradiation response, included as a biological reference rather than as a single-cohort fit. **(E) TD compartment dynamics during regeneration.** The effective TD pool initially declines after injury and subsequently recovers as the system returns to the homeostatic composition. **(F) Recovery of stem frequency.** The stem fraction  $s(t)$  returns toward the Nash/homeostatic frequency  $s^* = 0.0479$  after injury-induced depletion, illustrating that regeneration restores not only total abundance but also the homeostatic phenotypic composition. The biological context for the calibration is the murine small-intestinal crypt, in which Lgr5<sup>+</sup> CBC stem cells divide approximately once per day and the epithelium renews on a 4–5 day timescale.

compared against a semi-quantitative reconstruction of the published post-irradiation response rather than a single harmonized cohort.

The key qualitative prediction is that recovery of the stem pool is driven initially by the return flux  $\lambda_R(\bar{P})\bar{W}$  from the TD compartment rather than by net self-renewal of the depleted stem population. This is consistent with the mechanism highlighted experimentally by Murata et al. (Murata et al. 2020), who showed that regeneration of the ablated ISC compartment is explained to a large extent by dedifferentiation of

absorptive and secretory progenitors and requires ASCL2 activity. Within the reduced model, the same biology appears as a transient regime in which the stem frequency falls below  $s^*$  after injury, generating a positive payoff difference  $F_P - F_W$  and driving the system back toward the homeostatic composition. Figure 15 shows dedifferentiation as the dominant regenerative mechanism in the calibrated crypt model.

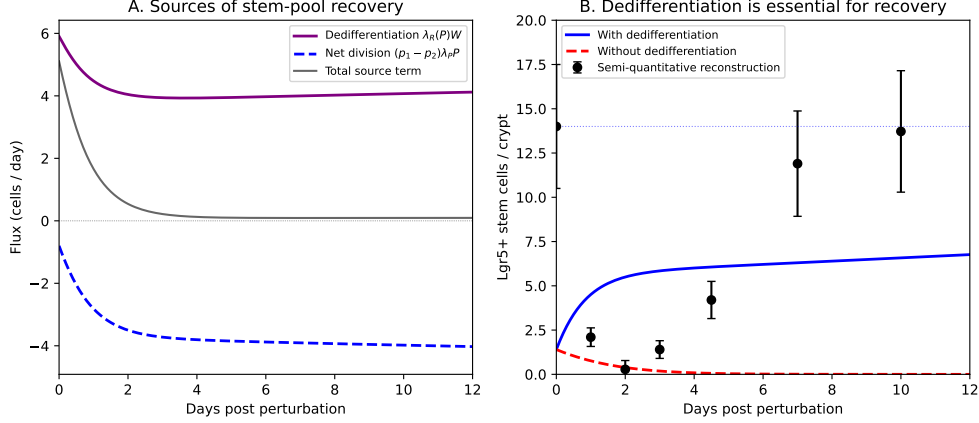


**Fig. 15 Dedifferentiation is the dominant regenerative mechanism in the calibrated crypt model. (A) Source decomposition of stem recovery.** During the early recovery phase after irradiation-like depletion, the dominant positive contribution to stem restoration is the dedifferentiation flux  $\lambda_R(\bar{P})\bar{W}$ , whereas the net division contribution  $(p_1 - p_2)\lambda_P\bar{P}$  is comparatively smaller and can remain negative during severe depletion. The total stem source term is their sum. **(B) Recovery with and without dedifferentiation.** Starting from the same post-injury depleted initial state, the full model (with dedifferentiation) restores the stem pool toward homeostasis, whereas the comparison model with  $\lambda_R \equiv 0$  fails to recover the stem compartment. This mirrors the biological picture in which intestinal regeneration after stem-cell ablation depends strongly on progenitor-cell plasticity and ASCL2-dependent dedifferentiation. The comparison should be interpreted as an intervention on the regenerative dynamics from a common injury-depleted baseline, not as a claim that the no-dedifferentiation model shares the same pre-injury homeostatic state.

This interpretation yields a clean mechanistic statement: following injury, the crypt does not merely regrow; rather, it dynamically rebalances phenotypic payoffs until the homeostatic equalization condition is restored. The replicator rest point therefore organizes both steady maintenance and post-injury composition recovery.

## 7.6 Biological predictions

The calibrated case study yields three experimentally testable predictions.

First, the Ratio law predicts that perturbations to epithelial loss or shedding should induce a compensatory shift in the equilibrium stem-to-TD ratio according to

$$\frac{\bar{P}^*}{\bar{W}^*} = \frac{\delta}{\lambda_P(\bar{W}^*)}.$$

Thus, increasing the effective loss rate  $\delta$  should require either a larger stem fraction or a larger effective production rate to preserve crypt homeostasis.

Second, the Equalization law predicts the dedifferentiation flux required to maintain the homeostatic composition:

$$\lambda_R(\bar{P}^*) = \delta(p_2(\bar{W}^*) - p_1(\bar{W}^*)).$$

This provides a route for inferring otherwise hard-to-measure plasticity rates from aggregate abundance measurements combined with proliferation and loss assays.

Third, the extinction–growth threshold of Theorem 5.1 predicts a critical boundary in the balance between renewal bias and loss rate. In the crypt setting, this implies that sufficiently severe increases in epithelial attrition, or sufficiently strong suppression of regenerative plasticity, should move the tissue toward a collapse regime in which a positive homeostatic equilibrium no longer exists.

Figure 16 shows testable predictions of the calibrated intestinal-crypt case study.

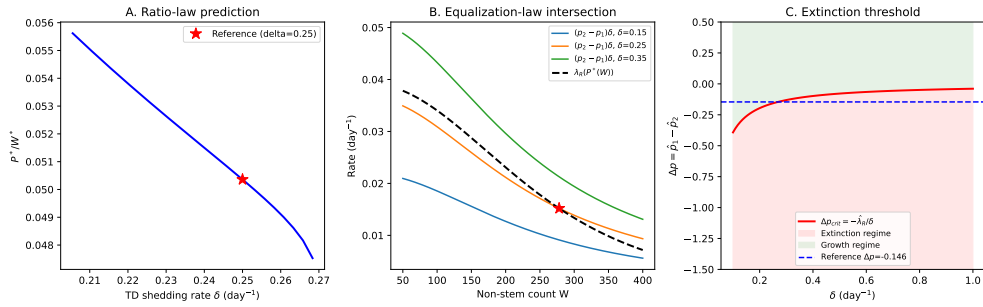


**Fig. 16 Testable predictions of the calibrated intestinal-crypt case study. (A) Ratio-law prediction.** The equilibrium stem/TD ratio varies systematically with the effective TD loss rate  $\delta$ , in accordance with  $\bar{P}^*/\bar{W}^* = \delta/\lambda_P(\bar{W}^*)$ . In the present coarse-grained model,  $\lambda_P(\bar{W}^*)$  is an aggregate effective production rate, so perturbations that alter epithelial loss or shedding are predicted to shift the equilibrium composition along this curve. **(B) Equalization-law geometry.** The homeostatic crypt state is determined by the intersection of the Ratio law and the Equalization law. The highlighted reference point marks the calibrated crypt equilibrium  $(\bar{P}^*, \bar{W}^*) = (14, 278)$ . **(C) Extinction–growth threshold.** The reduced model predicts a threshold separating extinction and growth regimes, controlled by the balance between renewal bias and effective loss. Increasing epithelial attrition or suppressing regenerative plasticity moves the system toward the collapse boundary at which no positive homeostatic equilibrium persists. Together, these panels show how the aggregate laws derived from the mechanistic model yield directly falsifiable predictions for crypt composition, regenerative compensation, and loss of tissue integrity.

## 7.7 Limitations of the crypt coarse-graining

The main biological limitation is the deliberate lumping of transit-amplifying cells into the effective TD compartment. This is why the calibrated  $\lambda_P(\bar{W}^*) \approx 4.9643 \text{ day}^{-1}$  should not be compared directly to the CBC single-cell cycling rate. A three-compartment stem/TA/TD extension would yield a more literal mapping to crypt

biology, but would also move the analysis away from the exact two-dimensional closure established here.

A second limitation is that the irradiation-recovery trajectories used in the figures are assembled as a semi-quantitative reconstruction from a literature spanning related but not identical experimental contexts. Accordingly, the regeneration comparison should be interpreted as a biologically grounded proof-of-principle case study rather than as a formal statistical fit to one harmonized single-cohort dataset.

With these caveats, the murine intestinal crypt provides a compelling proof-of-principle system: the aggregate homeostatic numbers are realistic, the injury-recovery mechanism is biologically documented, and the induced game-theoretic laws generate concrete, falsifiable predictions for how plasticity and feedback stabilize tissue maintenance.

## 8 Discussion

### *Experimental interpretation of the homeostatic laws.*

At homeostasis, Eqs. (16)–(17) can be read as two directly measurable balance statements. First, the Ratio Law,  $\bar{P}^*/\bar{W}^* = \delta/\lambda_P(\bar{W}^*)$ , predicts that the observed steady-state stem fraction is determined by a competition between TD clearance and the effective stem-cycle rate. The TD clearance rate,  $\delta$ , can be measured using labeled-cohort survival or apoptosis assays. The effective stem-cycle rate at the resident differentiated load,  $\lambda_P(\bar{W}^*)$ , can be estimated from EdU/BrdU incorporation, mitotic index, or time-lapse lineage tracking stratified by  $\bar{W}^*$ . Second, the Equalization Law,  $\lambda_R(\bar{P}^*) = \delta(p_2(\bar{W}^*) - p_1(\bar{W}^*))$ , predicts the magnitude of the TD-to-stem return flux required to maintain a steady tissue composition. Experimentally,  $\lambda_R(\bar{P}^*)$  can be inferred from fate-mapping or lineage tracing studies that quantify the rate at which marker-positive TD cells re-enter the stem compartment under steady-state conditions or following controlled micro-injury. Together, these relations imply a concrete perturbation logic. If plasticity is experimentally increased (e.g. injury cues that raise effective TD→stem return), the steady ratio must shift along the algebraic curves in Fig. 4. Conversely, if apoptosis or clearance  $\delta$  is increased, the laws predict both the direction and magnitude of the compensatory shift in compartment sizes required to preserve equilibrium. The extinction–growth threshold (Theorem 5.1) provides an orthogonal assay: depletion or repopulation experiments should display a sharp recovery vs. collapse boundary as renewal bias is tuned.

### 8.1 Limitation and Extension

#### *On the assumption of uniform mortality*

Our derivation of the exact evolutionary game relies on the assumption of damage-independent mortality ( $\delta(x) \equiv \delta$ ). Biologically, this regime corresponds to tissues where cell removal is driven primarily by extrinsic stochastic factors. Examples include mechanical shedding in the intestinal epithelium (Blander 2016; Williams et al. 2015), random differentiation-linked loss, or environmental fluctuations, rather than the gradual accumulation of intracellular toxicity. In the context of “neutral drift” models of

stem cell homeostasis (Xu et al. 2018; Traulsen et al. 2013), clonal extinction is often modeled as a random process independent of fitness, aligning with our uniform rate hypothesis.

While strictly damage-dependent mortality ( $\delta'(x) > 0$ ) would prevent the exact closure of the moment equations, it does not necessarily destroy the homeostatic stability. We argue that our reduced system captures the dominant order parameter (total tissue mass) dynamics. The analytical transparency gained by this simplification allows us to derive the explicit Equalization and Ratio Laws, offering a theoretical benchmark. Future work using moment-closure approximations could extend this framework to include weak damage-dependent mortality as a perturbation to this exact solution.

A natural extension is to incorporate intrinsic demographic fluctuations in division/death events. If spatial transport is introduced, one may seek a spectral analogue of the present scalar threshold laws. Recent mode-wise analyses of coupled mass-transport systems show that reciprocal feedback can be reduced to explicit Laplacian-mode instability criteria (Yu et al. 2026b). Recent chemical-Langevin work derived directly from continuous-time-Markov-chain event structure shows how to combine full state-dependent covariance, absorbing boundaries, and strong well-posedness in extinction-permitting population systems (Yu et al. 2026). For stochastic population models, stochastic differential equation toolkits can provide well-posedness, moment control, and Lyapunov-type bounds (e.g., (Wang and Yu 2025)). More generally, any stochastic extension of the present lineage model should be covariance-consistent at the event level rather than built from ad hoc diagonal noise. Recent mechanistic diffusion analyses emphasize that cross-covariance structure is dictated by channel stoichiometry and that open-domain and extinction-permitting absorbed formulations should be distinguished explicitly (Yu and Wang 2026). These tools could be combined with our exact closure to quantify how noise perturbs the ratio, equalization, and threshold predictions.

## Appendix A Technical lemmas and estimates

### A.1 Notation and auxiliary bounds

For  $T > 0$  we work in

$$\mathcal{X}_T := C([0, T]; L^1([0, \infty)) \times L^1([0, \infty))), \quad \|(P, W)\|_{\mathcal{X}_T} := \sup_{t \in [0, T]} (\|P(t, \cdot)\|_1 + \|W(t, \cdot)\|_1).$$

Throughout,  $\|\cdot\|_1$  denotes the  $L^1([0, \infty))$  norm, and we write

$$\bar{P}(t) = \|P(t, \cdot)\|_1, \quad \bar{W}(t) = \|W(t, \cdot)\|_1.$$

Let  $p_3(\cdot) = 1 - p_1(\cdot) - p_2(\cdot)$ . Under Assumption 2.1, the feedback maps are bounded and Lipschitz on  $[0, \infty)$ . We set the global bounds

$$0 \leq p_i(\cdot) \leq \hat{p}_i, \quad 0 \leq p_3(\cdot) \leq 1, \quad 0 \leq \lambda_P(\cdot) \leq \hat{\lambda}_P, \quad 0 \leq \lambda_R(\cdot) \leq \hat{\lambda}_R, \quad (\text{A1})$$

and the global Lipschitz constants

$$L_{p_1} := \sup_{x \geq 0} |p'_1(x)|, \quad L_{p_2} := \sup_{x \geq 0} |p'_2(x)|, \quad L_{\lambda_P} := \sup_{x \geq 0} |\lambda'_P(x)|, \quad L_{\lambda_R} := \sup_{x \geq 0} |\lambda'_R(x)|. \quad (\text{A2})$$

Then  $p_3$  is Lipschitz with constant  $L_{p_3} := L_{p_1} + L_{p_2}$ .

## A.2 Kernel mass identities

A key structural ingredient in the balance-law reduction is that the nonlocal birth operators preserve  $L^1$ -mass in each deterministic inheritance branch.

**Lemma A.1** (Change-of-variables identity) *For any  $\alpha \in (0, 1)$  and any  $f \in L^1_+([0, \infty))$ ,*

$$\int_0^\infty \frac{1}{\alpha} f\left(\frac{x}{\alpha}\right) dx = \int_0^\infty f(y) dy. \quad (\text{A3})$$

*Proof* Set  $y = x/\alpha$ , so  $dx = \alpha dy$  and the integral becomes  $\int_0^\infty f(y) dy$ .  $\square$

**Lemma A.2** (Birth-operator mass formulas) *Let  $\mathcal{B}_P, \mathcal{B}_W$  be defined in (3). Then, for a.e.  $t \geq 0$ ,*

$$\int_0^\infty \mathcal{B}_P[P](t, x) dx = (2p_1(\bar{W}(t)) + p_3(\bar{W}(t))) \lambda_P(\bar{W}(t)) \bar{P}(t), \quad (\text{A4})$$

$$\int_0^\infty \mathcal{B}_W[P](t, x) dx = (2p_2(\bar{W}(t)) + p_3(\bar{W}(t))) \lambda_P(\bar{W}(t)) \bar{P}(t), \quad (\text{A5})$$

and therefore

$$\int_0^\infty (\mathcal{B}_P[P] + \mathcal{B}_W[P])(t, x) dx = 2 \lambda_P(\bar{W}(t)) \bar{P}(t). \quad (\text{A6})$$

*Proof* Apply Lemma A.1 term-by-term in (3) and use  $p_1 + p_2 + p_3 = 1$ .  $\square$

## A.3 Vanishing of transport boundary flux under homogeneous inflow

The following lemma formalizes why the boundary terms disappear when integrating the transport equations over  $x \geq 0$  under the homogeneous inflow condition.

**Lemma A.3** (Boundary flux cancellation) *Assume  $v > 0$  and  $u \in C([0, T]; L^1([0, \infty)))$  is a weak solution to  $\partial_t u + v \partial_x u = g$  on  $(0, T) \times (0, \infty)$  with homogeneous inflow boundary  $u(t, 0) = 0$  (in the trace sense) and  $g \in L^1((0, T); L^1)$ . Then, for a.e.  $t \in (0, T)$ ,*

$$\int_0^\infty v \partial_x u(t, x) dx = 0 \quad (\text{A7})$$

*in the distributional sense used to derive balance laws.*

*Proof sketch* Test the weak formulation against  $\psi_R(x)$  with  $\psi_R \equiv 1$  on  $[0, R]$ ,  $\text{supp } \psi_R \subset [0, R + 1]$ , and  $\|\psi'_R\|_\infty \leq C$  independent of  $R$ . Integration by parts yields the transport contribution  $v \int_0^\infty u(t, x) \psi'_R(x) dx$ , which vanishes as  $R \rightarrow \infty$  by dominated convergence and  $u(t, \cdot) \in L^1$ . The inflow boundary condition ensures there is no boundary injection at  $x = 0$ .  $\square$

#### A.4 Mild formulation and Picard contraction

We record a clean version of the mild formulation and a contraction estimate sufficient for local well-posedness.

Define characteristics

$$X_P(s; t, x) = x - v_P(t - s), \quad X_W(s; t, x) = x - v_W(t - s), \quad 0 \leq s \leq t,$$

and integrating factors

$$\Lambda_P(s; t) := \int_s^t \lambda_P(\bar{W}(\tau)) d\tau, \quad \Lambda_W(s; t, x) := \int_s^t (\delta(X_W(\tau; t, x)) + \lambda_R(\bar{P}(\tau))) d\tau.$$

For  $(P, W) \in \mathcal{X}_T$ , define  $\Psi(P, W) = (\tilde{P}, \tilde{W})$  by

$$\tilde{P}(t, x) = e^{-\Lambda_P(0; t)} P_0(x - v_P t) \mathbf{1}_{x \geq v_P t} + \int_0^t e^{-\Lambda_P(s; t)} \left( \mathcal{B}_P[P] + \lambda_R(\bar{P}(s)) W \right)(s, X_P(s; t, x)) \mathbf{1}_{x \geq v_P(t-s)} ds, \quad (\text{A8})$$

$$\tilde{W}(t, x) = e^{-\Lambda_W(0; t, x)} W_0(x - v_W t) \mathbf{1}_{x \geq v_W t} + \int_0^t e^{-\Lambda_W(s; t, x)} \mathcal{B}_W[P](s, X_W(s; t, x)) \mathbf{1}_{x \geq v_W(t-s)} ds. \quad (\text{A9})$$

**Lemma A.4** (Local contraction estimate) *Let  $M_0 := \|P_0\|_1 + \|W_0\|_1$  and consider the closed ball  $\mathbb{B}(0, 2M_0) \subset \mathcal{X}_T$ . There exists a constant  $C = C(M_0)$ , depending only on  $M_0$ , the bounds (A1), and the Lipschitz constants (A2), such that for all  $(P_j, W_j) \in \mathbb{B}(0, 2M_0)$ ,*

$$\|\Psi(P_1, W_1) - \Psi(P_2, W_2)\|_{\mathcal{X}_T} \leq C(T + T^2) \|(P_1, W_1) - (P_2, W_2)\|_{\mathcal{X}_T}. \quad (\text{A10})$$

*In particular, for  $T > 0$  sufficiently small so that  $C(T + T^2) < 1$ ,  $\Psi$  is a strict contraction on  $\mathbb{B}(0, 2M_0)$ .*

*Proof skeleton* The proof proceeds term-by-term in (A8)–(A9): (i) differences of exponentials are bounded by integrals of coefficient differences, using the mean value theorem and Lipschitz continuity; (ii) the nonlocal birth terms satisfy

$$\left\| \frac{1}{\alpha} P(\cdot, \cdot / \alpha) \right\|_{L^1} = \|P\|_{L^1}$$

by Lemma A.1, and coefficient differences, controlled by the Lipschitz property of  $\lambda_P$  and the uniform bound  $\|P\|_1 \leq 2M_0$  on the ball, contribute at most  $\mathcal{O}(T)$ ; (iii) nested time integrals yield the  $\mathcal{O}(T^2)$  term. All bounds close on  $\mathbb{B}(0, 2M_0)$  because  $\bar{P}, \bar{W}$  are uniformly bounded by  $2M_0$  on this set.  $\square$

## A.5 A priori mass estimate (global continuation)

Finally, we record the  $L^1$  mass bound used to extend local solutions globally.

**Lemma A.5** (Mass bound) *Let  $(P, W)$  be a nonnegative mild solution on  $[0, T]$  under Assumption 2.1. Define  $M(t) := \|P(t)\|_1 + \|W(t)\|_1$ . Then*

$$M(t) \leq M(0) e^{\hat{\lambda}_P t}, \quad t \in [0, T], \quad (\text{A11})$$

where  $\hat{\lambda}_P = \lambda_P(0)$ .

*Proof* Integrate the PDEs over  $x \geq 0$  using Lemmas A.2 and A.3. Nonnegativity and  $\lambda_P(\bar{W}) \leq \hat{\lambda}_P$  yield  $\dot{M}(t) \leq \hat{\lambda}_P P(t) \leq \hat{\lambda}_P M(t)$ , hence (A11) by Grönwall.  $\square$

**Acknowledgments:** The authors confirm that this research received no external funding.

**Author contributions:** Both authors contributed equally to this article and as Co-First Authors. Both two authors read and approved the final manuscript

**Competing interests:** The authors declare that they have no conflict of interest.

**Data availability:** Data sharing is not applicable to this article as no datasets were generated or analyzed during the current study.

## References

- Argasinski, K., Broom, M.: Interaction rates, vital rates, background fitness and replicator dynamics: how to embed evolutionary game structure into realistic population dynamics. *Theory in Biosciences* **137**(1), 33–50 (2018) <https://doi.org/10.1007/s12064-017-0257-y>
- Beumer, J., Clevers, H.: Regulation and plasticity of intestinal stem cells during homeostasis and regeneration. *Development* **143**(20), 3639–3649 (2016) <https://doi.org/10.1242/dev.133132>
- Blanpain, C., Fuchs, E.: Plasticity of epithelial stem cells in tissue regeneration. *Science* **344**(6189), 1242281 (2014) <https://doi.org/10.1126/science.1242281>
- Bates, J.H.T., Herrmann, J., Casey, D.T., Suki, B.: An agent-based model of tissue maintenance and self-repair. *American Journal of Physiology-Cell Physiology* **324**(4), 941–950 (2023) <https://doi.org/10.1152/ajpcell.00531.2022>
- Biteau, B., Hochmuth, C.E., Jasper, H.: Maintaining tissue homeostasis: dynamic control of somatic stem cell activity. *Cell Stem Cell* **9**(5), 402–411 (2011) <https://doi.org/10.1016/j.stem.2011.10.004>

- Bensellam, M., Jonas, J.-C., Laybutt, D.R.: Mechanisms of  $\beta$ -cell dedifferentiation in diabetes: recent findings and future research directions. *Journal of Endocrinology* **236**(2), 109–143 (2018) <https://doi.org/10.1530/JOE-17-0516>
- Blander, J.M.: Death in the intestinal epithelium—basic biology and implications for inflammatory bowel disease. *The FEBS Journal* **283**(14), 2720–2730 (2016) <https://doi.org/10.1111/febs.13771>
- Bose, B., Nihad, M., P, S.S.: Pluripotent stem cells: Basic biology or else differentiations aimed at translational research and the role of flow cytometry. *Cytometry Part A* **103**(5), 368–377 (2023) <https://doi.org/10.1002/cyto.a.24726>
- Chen, C.W.: Estimating birth and death rates from cell labeling data. *Stochastic Environmental Research and Risk Assessment* **23**(5), 621–626 (2009) <https://doi.org/10.1007/s00477-008-0247-1>
- Chiacchiera, F.: Transcriptional and epigenetic mechanisms controlling intestinal cell fate. In: *Epigenetics and Regeneration*, pp. 259–286. Elsevier, London (2019). <https://doi.org/10.1016/B978-0-12-814879-2.00011-X>
- Cui, M., Lv, Y., Pan, H., Yang, L.: Hopf-bifurcation analysis of a stage-structured population model of cell differentiation. *Physica D: Nonlinear Phenomena* **467**, 134266 (2024) <https://doi.org/10.1016/j.physd.2024.134266>
- Crowley, L.C., Marfell, B.J., Scott, A.P., Waterhouse, N.J.: Quantitation of apoptosis and necrosis by annexin V binding, propidium iodide uptake, and flow cytometry. *Cold Spring Harbor Protocols* **2016**(11), 087288 (2016) <https://doi.org/10.1101/pdb.prot087288>
- Cressman, R., Tao, Y.: The replicator equation and other game dynamics. *Proceedings of the National Academy of Sciences* **111**(supplement\_3), 10810–10817 (2014) <https://doi.org/10.1073/pnas.1400823111>
- Chatterjee, B., Thakur, S.S.: Aging of hematopoietic stem cells: Insight into mechanisms and consequences. In: *Stem Cells and Aging*, pp. 103–111. Elsevier, London (2021). <https://doi.org/10.1016/B978-0-12-820071-1.00016-5>
- Daluiski, A., Engstrand, T., Bahamonde, M.E., Gamer, L.W., Agius, E., Stevenson, S.L.: Bone morphogenetic protein-3 is a negative regulator of bone density. *Nature Genetics* **27**(1), 84–88 (2001) <https://doi.org/10.1038/83810>
- Dieckmann, U., Law, R.: The dynamical theory of coevolution: a derivation from stochastic ecological processes. *Journal of Mathematical Biology* **34**(5-6), 579–612 (1996) <https://doi.org/10.1007/BF02409751>
- Dercole, F., Rinaldi, S.: *Analysis of Evolutionary Processes: the Adaptive Dynamics Approach and Its Applications*. Princeton series in theoretical and computational

- biology. Princeton University Press, Princeton (2008)
- Gall, L., Duckworth, C., Jardi, F., Lammens, L., Parker, A., Bianco, A.: Homeostasis, injury, and recovery dynamics at multiple scales in a self-organizing mouse intestinal crypt. *eLife* **12**, 85478 (2023) <https://doi.org/10.7554/eLife.85478>
- Geritz, S.A.H., Kisdi, E., Mesze´NA, G., Metz, J.A.J.: Evolutionarily singular strategies and the adaptive growth and branching of the evolutionary tree. *Evolutionary Ecology* **12**(1), 35–57 (1998) <https://doi.org/10.1023/A:1006554906681>
- Guillot, C., Lecuit, T.: Mechanics of epithelial tissue homeostasis and morphogenesis. *Science* **340**(6137), 1185–1189 (2013) <https://doi.org/10.1126/science.1235249>
- Guo, Y., Wu, W., Yang, X., Fu, X.: Dedifferentiation and *in vivo* reprogramming of committed cells in wound repair. *Molecular Medicine Reports* **26**(6), 369 (2022) <https://doi.org/10.3892/mmr.2022.12886>
- Helbing, D.: A stochastic behavioral model and a ‘Microscopic’ foundation of evolutionary game theory. *Theory and Decision* **40**(2), 149–179 (1996) <https://doi.org/10.1007/BF00133171>
- Huang, W., Hauert, C., Traulsen, A.: Stochastic game dynamics under demographic fluctuations. *Proceedings of the National Academy of Sciences* **112**(29), 9064–9069 (2015) <https://doi.org/10.1073/pnas.1418745112>
- Huelsz-Prince, G., Kok, R.N.U., Goos, Y., Bruens, L., Zheng, X., Ellenbroek, S.: Mother cells control daughter cell proliferation in intestinal organoids to minimize proliferation fluctuations. *eLife* **11**, 80682 (2022) <https://doi.org/10.7554/eLife.80682>
- Hofbauer, J., Sigmund, K.: *Evolutionary Games and Population Dynamics*, 1st edn. Cambridge University Press, Cambridge (1998). <https://doi.org/10.1017/CBO9781139173179>
- Hagemann, R., Sigdestad, C., Leshner, S.: Quantitation of intestinal villus cells on a weight basis: values for C57BL-6 mice. *American Journal of Physiology-Legacy Content* **218**(3), 637–640 (1970) <https://doi.org/10.1152/ajplegacy.1970.218.3.637>
- Jopling, C., Boue, S., Belmonte, J.C.I.: Dedifferentiation, transdifferentiation and reprogramming: three routes to regeneration. *Nature Reviews Molecular Cell Biology* **12**(2), 79–89 (2011) <https://doi.org/10.1038/nrm3043>
- Jones, L., Passegue, E.: Stem cells homeostasis and aging. *Innovation in Aging* **7**(Supplement.1), 259–260 (2023) <https://doi.org/10.1093/geroni/igad104.0862>
- Lou, Y., Chen, A., Yoshida, E., Chen, Y.: Homeostasis and systematic ageing as non-equilibrium phase transitions in computational multicellular organizations. *Royal*

- Society Open Science **6**(7), 190012 (2019) <https://doi.org/10.1098/rsos.190012>
- Liu, B., Qu, J., Zhang, W., Izipisua Belmonte, J.C., Liu, G.-H.: A stem cell aging framework, from mechanisms to interventions. *Cell Reports* **41**(3), 111451 (2022) <https://doi.org/10.1016/j.celrep.2022.111451>
- Liu, Z., Wang, L.S., Yu, J., Zhang, J., Martel, E., Li, S.: Bidirectional endothelial feedback drives turing-vascular patterning and drug-resistance niches: a hybrid PDE-agent-based study. *Bioengineering* **12**(10), 1097 (2025) <https://doi.org/10.3390/bioengineering12101097>
- Liang, Y., Wang, L.S., Yu, J., Liu, Z.: Global well-posedness and stability of nonlocal damage-structured lineage model with feedback and dedifferentiation. *Mathematics* **13**(22), 3583 (2025) <https://doi.org/10.3390/math13223583>
- Metz, J.A.J., Geritz, S.A.H., Meszner, G., Jacobs, F.J.A., Heerwaarden, J.S.: Adaptive dynamics: a geometrical study of the consequences of nearly faithful reproduction. In: *Iiasa Studies in Adaptive Dynamics*, (1995). <https://pure.iiasa.ac.at/id/eprint/4497/> Accessed 2026-02-16
- Mi, L., Hu, J., Li, N., Gao, J., Huo, R., Peng, X.: The mechanism of stem cell aging. *Stem Cell Reviews and Reports* **18**(4), 1281–1293 (2022) <https://doi.org/10.1007/s12015-021-10317-5>
- Murata, K., Jadhav, U., Madha, S., Van Es, J., Dean, J., Cavazza, A.: Ascl2-dependent cell dedifferentiation drives regeneration of ablated intestinal stem cells. *Cell Stem Cell* **26**(3), 377–3906 (2020) <https://doi.org/10.1016/j.stem.2019.12.011>
- McPherron, A.C., Lawler, A.M., Lee, S.-J.: Regulation of skeletal muscle mass in mice by a new TGF- $\beta$  superfamily member. *Nature* **387**(6628), 83–90 (1997) <https://doi.org/10.1038/387083a0>
- McNeely, T., Leone, M., Yanai, H., Beerman, I.: DNA damage in aging, the stem cell perspective. *Human Genetics* **139**(3), 309–331 (2020) <https://doi.org/10.1007/s00439-019-02047-z>
- Magal, P., Ruan, S.: *Theory and Applications of Abstract Semilinear Cauchy Problems*. Applied Mathematical Sciences, vol. 201. Springer, Cham (2018). <https://doi.org/10.1007/978-3-030-01506-0>
- Nordmann, T.M., Dror, E., Schulze, F., Traub, S., Berishvili, E., Barbieux, C.: The role of inflammation in  $\beta$ -cell dedifferentiation. *Scientific Reports* **7**(1), 6285 (2017) <https://doi.org/10.1038/s41598-017-06731-w>
- Oh, J., Lee, Y.D., Wagers, A.J.: Stem cell aging: mechanisms, regulators and therapeutic opportunities. *Nature Medicine* **20**(8), 870–880 (2014) <https://doi.org/10.1038/nm.3651>

- Oberkampf, W.L., Trucano, T.G.: Verification and validation in computational fluid dynamics. *Progress in Aerospace Sciences* **38**(3), 209–272 (2002) [https://doi.org/10.1016/S0376-0421\(02\)00005-2](https://doi.org/10.1016/S0376-0421(02)00005-2)
- Perko, L.: *Differential Equations and Dynamical Systems. Texts in Applied Mathematics*, vol. 7. Springer, New York, NY (2001). <https://doi.org/10.1007/978-1-4613-0003-8>
- Perthame, B.: *Transport Equations in Biology. Frontiers in Mathematics*. Birkhäuser Basel, Basel (2007). <https://doi.org/10.1007/978-3-7643-7842-4>
- Perthame, B.: *Introduction to structured equations in biology* (2023). Accessed 2026-02-14
- Roache, P.J.: *Verification and Validation in Computational Science and Engineering*. Hermosapublishers, Albuquerque, N.M (1998)
- Richmond, C.A., Shah, M.S., Carlone, D.L., Breault, D.T.: An enduring role for quiescent stem cells. *Developmental Dynamics* **245**(7), 718–726 (2016) <https://doi.org/10.1002/dvdy.24416>
- Schuster, P., Sigmund, K.: Replicator dynamics. *Journal of Theoretical Biology* **100**(3), 533–538 (1983) [https://doi.org/10.1016/0022-5193\(83\)90445-9](https://doi.org/10.1016/0022-5193(83)90445-9)
- Snippert, H.J., Van Der Flier, L.G., Sato, T., Van Es, J.H., Van Den Born, M., Kroon-Veenboer, C.: Intestinal crypt homeostasis results from neutral competition between symmetrically dividing Lgr5 stem cells. *Cell* **143**(1), 134–144 (2010) <https://doi.org/10.1016/j.cell.2010.09.016>
- Safina, K., Van Galen, P.: New frameworks for hematopoiesis derived from single-cell genomics. *Blood* **144**(10), 1039–1047 (2024) <https://doi.org/10.1182/blood.2024024006>
- Tetteh, P.W., Basak, O., Farin, H.F., Abbott, K.C., Kretzschmar, K., Begthel, H.: Replacement of lost Lgr5-positive stem cells through plasticity of their enterocyte-lineage daughters. *Cell Stem Cell* **18**(2), 203–213 (2016) <https://doi.org/10.1016/j.stem.2016.01.001>
- Tzeng, Y.-S., Li, H., Kang, Y.-L., Chen, W.-C., Cheng, W.-C., Lai, D.-M.: Loss of Cxcl12/Sdf-1 in adult mice decreases the quiescent state of hematopoietic stem/progenitor cells and alters the pattern of hematopoietic regeneration after myelosuppression. *Blood* **117**(2), 429–439 (2011) <https://doi.org/10.1182/blood-2010-01-266833>
- Traulsen, A., Lenaerts, T., Pacheco, J.M., Dingli, D.: On the dynamics of neutral mutations in a mathematical model for a homogeneous stem cell population. *Journal of The Royal Society Interface* **10**(79), 20120810 (2013) <https://doi.org/10.1098/>

- Tata, P.R., Mou, H., Pardo-Saganta, A., Zhao, R., Prabhu, M., Law, B.M.: Dedifferentiation of committed epithelial cells into stem cells in vivo. *Nature* **503**(7475), 218–223 (2013) <https://doi.org/10.1038/nature12777>
- Van Der Flier, L.G., Clevers, H.: Stem cells, self-renewal, and differentiation in the intestinal epithelium. *Annual Review of Physiology* **71**(1), 241–260 (2009) <https://doi.org/10.1146/annurev.physiol.010908.163145>
- Van Der Heijden, M., Vermeulen, L.: Stem cells in homeostasis and cancer of the gut. *Molecular Cancer* **18**(1), 66 (2019) <https://doi.org/10.1186/s12943-019-0962-x>
- Vadakke-Madathil, S., Limaye, L.S., Kale, V.P., Chaudhry, H.W.: Flow cytometry and cell sorting using hematopoietic progenitor cells. In: *Progenitor Cells* vol. 2029, pp. 235–246. Springer, New York, NY (2019). [https://doi.org/10.1007/978-1-4939-9631-5\\_18](https://doi.org/10.1007/978-1-4939-9631-5_18)
- Williams, J.M., Duckworth, C.A., Burkitt, M.D., Watson, A.J.M., Campbell, B.J., Pritchard, D.M.: Epithelial cell shedding and barrier function: a matter of life and death at the small intestinal villus tip. *Veterinary Pathology* **52**(3), 445–455 (2015) <https://doi.org/10.1177/0300985814559404>
- Wu, H.-H., Ivkovic, S., Murray, R.C., Jaramillo, S., Lyons, K.M., Johnson, J.E.: Autoregulation of neurogenesis by GDF11. *Neuron* **37**(2), 197–207 (2003) [https://doi.org/10.1016/S0896-6273\(02\)01172-8](https://doi.org/10.1016/S0896-6273(02)01172-8)
- Weinberg, N., Ouziel-Yahalom, L., Knoller, S., Efrat, S., Dor, Y.: Lineage tracing evidence for in vitro dedifferentiation but rare proliferation of mouse pancreatic  $\beta$ -cells. *Diabetes* **56**(5), 1299–1304 (2007) <https://doi.org/10.2337/db06-1654>
- Wang, L.S., Yu, J.: Analysis framework for stochastic predator–prey model with demographic noise. *Results in Applied Mathematics* **27**, 100621 (2025) <https://doi.org/10.1016/j.rinam.2025.100621>
- Wang, L.S., Yu, J.: Algebraic–spectral thresholds and discrete–continuous stability transfer in Leslie–Gower systems. *Electronic Research Archive* **34**(1), 251–290 (2026) <https://doi.org/10.3934/era.2026013>
- Wang, L.S., Yu, J., Liu, Z.: A damage-structured PDE model of stem cell hierarchies: The dual role of dedifferentiation in tissue homeostasis and aging. *PLOS One* **21**(2), 0335163 (2026) <https://doi.org/10.1371/journal.pone.0335163>
- Wang, L.S., Yu, J., Li, S., Liu, Z.: Analysis and mean-field limit of a hybrid PDE-ABM modeling angiogenesis-regulated resistance evolution. *Mathematics* **13**(17), 2898 (2025) <https://doi.org/10.3390/math13172898>

- Xavier Da Silveira Dos Santos, A., Liberali, P.: From single cells to tissue self-organization. *The FEBS Journal* **286**(8), 1495–1513 (2019) <https://doi.org/10.1111/febs.14694>
- Xu, S., Kim, S., Chen, I.S.Y., Chou, T.: Modeling large fluctuations of thousands of clones during hematopoiesis: The role of stem cell self-renewal and bursty progenitor dynamics in rhesus macaque. *PLOS Computational Biology* **14**(10), 1006489 (2018) <https://doi.org/10.1371/journal.pcbi.1006489>
- Yamasaki, K., Toriu, N., Hanakawa, Y., Shirakata, Y., Sayama, K., Takayanagi, A.: Keratinocyte growth inhibition by high-dose epidermal growth factor is mediated by transforming growth factor  $\beta$  autoinduction: a negative feedback mechanism for keratinocyte growth. *Journal of Investigative Dermatology* **120**(6), 1030–1037 (2003) <https://doi.org/10.1046/j.1523-1747.2003.12239.x>
- Yu, J., Wang, L.S.: Beyond diagonal noise: A better predator-prey modeling framework with cross-covariance. arXiv. Version Number: 1 (2026). <https://doi.org/10.48550/ARXIV.2602.22489>
- Yu, J., Wang, L.S., Gao, Y., Liang, Y.: Full-covariance chemical langevin predator-prey diffusion with absorbing boundaries. arXiv. Version Number: 1 (2026). <https://doi.org/10.48550/ARXIV.2602.05336>
- Yu, J., Wang, L.S., Liang, Y.: Dedifferentiation stabilizes stem cell lineages: From CTMC to diffusion theory and thresholds. arXiv. Version Number: 1 (2026). <https://doi.org/10.48550/ARXIV.2601.09752>
- Yu, J., Wang, L.S., Liu, Z., Liu, J.: Chemotactic feedback controls patterning in hybrid tumor-stroma model. arXiv. Version Number: 1 (2026). <https://doi.org/10.48550/ARXIV.2601.16337>
- Yu, J., Wang, L.S., Liu, Z., Liu, J.: Mode-wise spectral criteria for coupled mass transport in hybrid PDE-ODE tumor microenvironments. arXiv. Version Number: 1 (2026). <https://doi.org/10.48550/ARXIV.2601.20204>
- Zhao, J.L., Baltimore, D.: Regulation of stress-induced hematopoiesis. *Current Opinion in Hematology* **22**(4), 286–292 (2015) <https://doi.org/10.1097/MOH.000000000000149>
- Zhu, X., Jiang, L., Ye, M., Sun, L., Gagnoli, C., Wu, R.: Integrating evolutionary game theory into mechanistic genotype-phenotype mapping. *Trends in Genetics* **32**(5), 256–268 (2016) <https://doi.org/10.1016/j.tig.2016.02.004>
- Zhang, X., Liu, Z.: Periodic oscillations in age-structured ratio-dependent predator-prey model with michaelis-menten type functional response. *Physica D: Nonlinear Phenomena* **389**, 51–63 (2019) <https://doi.org/10.1016/j.physd.2018.10.002>